Preparation and optimization of TiO_2 photoanodes fabricated by pulsed laser deposition for photoelectrochemical water splitting

Roberto Matarrese[a], Isabella Nova*[a], Andrea Li Bassi[b], Carlo S. Casari[b],

Valeria Russo[b], Simonetta Palmas[c]

[a]Laboratory of Catalysis and Catalytic Processes, Dipartimento di Energia, Politecnico di Milano, via La Masa 34, 20156, Milano, Italy

[b]Micro- and Nanostructured Materials Lab., Dipartimento di Energia, Politecnico di Milano, via Ponzio 34/3, 20133, Milano, Italy

[c] Dipartimento di Ingegneria Meccanica, Chimica e dei Materiali, Università degli Studi di Cagliari, Via Marengo 3, 09123 Cagliari, Italy

***corresponding author**

Isabella Nova

Laboratory of Catalysis and Catalytic Processes

Dipartimento di Energia,

Politecnico di Milano

via La Masa 34

20156 Milano, Italia

e-mail isabella.nova@polimi.it

Abstract

Quasi-1D TiO_2 nanostructures prepared by Pulsed Laser Deposition (PLD) are tested as photoanodes for photoelectrochemical water splitting application and compared with TiO_2 nanotube arrays prepared by anodic oxidation. PLD TiO_2 films with controlled structure and morphology ranging from compact to vertically oriented or hierarchical porous nanostructures are deposited by ablating a TiO_2 target with ns UV laser pulses in the presence of O_2 background atmosphere at different pressures. Thermal treatments at different temperatures are used to transform the so-obtained amorphous systems into nanocrystalline structures (mainly anatase). The effect of film density and thickness are also considered by depositing different amounts of material per unit surface. The morphology and the phase composition of the samples are characterized by SEM and Raman Spectroscopy, while the photoelectrochemical water splitting performances are investigated by monitoring the photocurrent generated under illumination in a three-electrode cell. Voltammetric scans and EIS analysis were also used to correlate the morphology of PLD samples with their electrochemical properties and their working mechanism in the absence and presence of a light radiation. A clear correlation between structural/morphological properties and photoelectrochemical behavior is found and ideal values of the synthesis parameters are identified, which allow the identification of the optimal quasi-1D nanoporous morphology for water splitting applications. The use of sacrificial organic reagents as hole scavengers was also considered to improve the photoelectrochemical performance of the samples.

Keywords

Photoelectrochemical water splitting, TiO_2, nanostructured materials, quasi-1D/hierarchical nanostructures, Pulsed Laser Deposition, sacrificial agent

Introduction

In recent years, the increasing environmental concerns and the rising energy demand have led to focus the attention on new and sustainable sources of energy. Many efforts are underway to develop ecologically clean technologies based on the applications of hydrogen as a fuel instead of fossil fuels [1,2]. In this context, the production of hydrogen by photocatalytic water splitting using solar energy represents a promising way to provide a clean and renewable energy resource [3-6].

In the 1970s Fujishima and Honda [7] reported for the first-time water splitting into H_2 and O_2 with a TiO_2 photoanode via the so-called photoelectrochemical (PEC) approach. The typical PEC cell consists of a semiconductor photoanode (e.g. TiO_2) and a metal counter electrode (usually Pt) which are connected through an external load. Photo-irradiation of the anode results in the formation of charge carriers (electron-hole pairs): the holes oxidize water to form O_2 on the anode while the electrons are channelled through the external circuit towards the cathode, where they reduce water to form H_2. Often, when the energetics of photoanode or cathode are not suitable for the process, an external voltage or chemical bias (i.e. by ΔpH) needs to be applied to effect water splitting [3].

Despite other metal oxide semiconductors, also with rather complex structures, have been investigated in PEC applications, TiO_2 still remains the most investigated photocatalyst because of its activity, low-cost, non-toxicity and chemical stability (i.e. corrosion-resistance) [8,9]. Unfortunately, the industrial exploitation of photocatalytic hydrogen production via water splitting over TiO_2 is still limited, the major problems being a poor activation by visible light and the low quantum efficiency of the process, also related to the high degree of recombination between the photogenerated charges carriers (electron-hole pairs) [10]. In this regard, various strategies have been proposed to improve the PEC performance of TiO_2, such as TiO_2 doping/sensitization to enhance visible light absorption [4,5,11-13], or controlling photocatalysts structure and morphology to enhance the active surface, to increase light harvesting and to minimize electron trapping and recombination probabilities [13,14].

In the latter case, several nanostructured TiO_2 networks (e.g. tubes [15-17], rods [18-20], wires [21,22], sponges [23,24]) emerged as promising materials that can be used as photoanodes in water photoelectrolysis cells. In particular, as summarized in very recent reviews [25-30], extensive research has been performed on TiO_2 nanotube arrays (T–NTs) because their unique high surface-to-volume ratios (even though not as high as those obtained with nanoparticle assemblies), ordered geometry and tunable morphologies are claimed for fast charge separation and transport, and electrolyte ions diffusion as well.

Recently, novel 3-D architectures consisting of quasi-1D hierarchical nanostructures have received attention for direct solar energy conversion, because of their advantages in combining (i) large surface area, (ii) light scattering due to the

presence of features of size comparable to visible wavelengths, (iii) mesopores for diffusion of molecules (e.g. electrolytes ions in the case of photoelectrochemical solar cells, pollutants or reagents in the case of photocatalysis), and also (iv) anisotropic morphology (similarly to nanotubes or nanowires) to ensure better electron transport towards the electrical contact [31,32]. Such structures, characterized by multiscale features or self-affine morphologies over different length scales (from the nano- to the micro-scale) through low energy assembling of fine nanoparticles, can be produced by carefully tuning the plasma expansion dynamics in a Pulsed Laser Deposition (PLD) process [33-36]. In particular, nanocrystalline tree-like TiO_2 hierarchical structures prepared by reactive PLD have been proposed for application in dye-sensitized solar cells (DSSCs), showing long electron lifetime with respect to back recombination and high performances in terms of ion liquid electrolytes diffusion [31]. Improved light harvesting has been observed even when hierarchical photoanodes were employed in solid state (polymeric) DSSCs [32]. Moreover, the potential photocatalytic efficacy of such quasi-1D, hierarchical TiO_2 architectures has been proved in the mineralization (i.e. oxidation) of stearic acid, as a model molecule [34].

In this work, by exploiting the versatility of the PLD deposition process, we focus on the potential of vertically oriented assemblies of TiO_2 nanoparticles as photoanodes for the photoelectrochemical water splitting process. In particular, the existing correlations between structural/morphological properties and photoelectrochemical behaviour are analysed with the aim of identifying the optimal structures for water splitting applications.

A preliminary assessment of the suitability of structures prepared by PLD for photoelectrochemical water splitting was synthetically presented in a previous communication [37]: herein, we aim at a more detailed and comprehensive investigation of the effect of the variation of the preparation conditions (i.e. pressure, deposited mass and annealing temperature), in order to deep inside the effect of crystalline structure and morphology (i.e. porosity and thickness), ranging from compact to vertically oriented or hierarchical nanostructures, and the photoelectrochemical behaviour, which is evaluated through photocurrent tests, voltammetric scans, and electrochemical impedance spectroscopy (EIS) analysis. Moreover, the behaviour of a TiO_2 nanotubular (i.e. a model vertical-oriented and non-hierarchical nanostructure) photonaode, prepared by anodic oxidation, is also considered for comparison purposes. Finally, the performances of the PLD grown photoanodes are here investigated in the presence of glycerol, ethylene glycol and ethanol which are used as model organic sacrificial reagents to improve the PEC performances. In fact, from a practical point of view, photo-reforming of organic solutions instead of photo-cleavage of pure water looks more advantageous because most water pollutants are organics, and in this way hydrogen production can be usefully combined with the purification of water [38]. Moreover, it has been demonstrated that under favourable conditions and in the presence of O_2, photoelectrochemical (PEC) cells can act as Photofuelcells (PFC), consuming an organic substance (i.e. the fuel), and utilizing light energy to produce electricity [39].

Experimental

Synthesis of TiO_2 photoanodes

TiO_2 nanostructured films have been deposited at room temperature by ablating a TiO_2 target with UV (λ=266 nm) laser pulses from a frequency quadrupled Nd:YAG Q-switched laser with a pulse duration of about 5-7 ns. The laser fluence on the target was set at about 2.5 J cm^{-2} with a spot size of about 3 mm^2. The ablation was performed in the presence of a fixed background gas pressure of pure oxygen (99.999%) which was varied in the 3-15 Pa range to control the material structure/morphology. Silicon, glass and Ti were used as substrates mounted on an off-axis rotating sample holder at a fixed target-to-substrate distance of 50 mm. TiO_2 films deposited on silicon and glass substrates were used for SEM and Raman characterization while those deposited on Ti for photoelectrochemical experiments (see below). Further details on the PLD experimental setup and procedures are reported in previous works [32-34]. In particular, those results demonstrated that the structure and morphology of TiO_2 films deposited by PLD can be tuned by controlling the pressure of the background gas, while other parameters, such as the target-to-substrate distance, the laser fluence and the gas flux have been previously set [33].

Ti plate substrates for photoelectrochemical measurements were masked to deposit on a 2x1 cm^2 area and to leave a clean surface for electrical contacts. All the substrates were kept at room temperature and no substrate heating was observed during deposition. The deposited mass per unit surface was measured by a quartz crystal microbalance at the same position as the substrates. In order to study the influence of thickness, films with a different mass per unit surface were deposited, i.e. 0.5*M*, *M* and 2*M* (where *M* is about 0.3-0.4 mg cm^{-2}), keeping constant the oxygen partial pressure during deposition (5 Pa). Post deposition thermal annealing processes were performed for 2 hours in air in a muffle furnace at 500 °C, 650 °C and 800 °C to induce crystalline order. In fact, as well known in literature [5,25,28], a high degree of crystallinity has positive effects on water splitting activity, mainly due to a decrease of defect concentration which reduces recombination between photogenerated carriers.

For comparison purpose, a TiO_2 nanotubes photoanode (TNT) was prepared through an electrochemical anodization method already tested in previous works [16, 40]. Briefly, starting from Titanium foil (0.25 mm thick, 99.7% metal basis, Aldrich) which was preliminarily degreased, the anodization was performed in water/glycerol solution containing NH_4F (Glycerol/H_2O 80:20 vol.% + 0.1 M NH_4F). A potential ramp was applied from open-circuit voltage (OCV) to a fixed potential (20 V) with a scan rate of 100 mV s^{-1}; then, the applied potential was maintained at this fixed value for 3 h. After oxidation, the sample was rinsed in deionized water, dried in a nitrogen stream and subsequently thermally treated in air at 400 °C for 1 h.

Morphological and structural characterization

PLD grown films morphology was observed with a ZEISS Supra 40 FEG-SEM without any sample preparation. SEM analyses (top view and cross sectional) were performed on TiO_2 films obtained on silicon substrates. Film density was evaluated by combining information on the deposited mass per unit surface with thickness measurements by cross-sectional SEM images ($\rho_{film}=M\ h^{-1}$ where M is the mass/cm^2 and h is the film thickness). The porosity of the systems has been then estimated as percentage of voids and evaluated from the ratio between film density and bulk anatase density ($1-\rho_{film}/\rho_{bulk}$), with $\rho_{bulk} = 3.9$ g cm^{-3}.

The crystalline structure of the PLD films obtained from TiO_2 on glass/silicon was characterized by Raman spectroscopy using a Renishaw InVia micro Raman spectrometer with 514.5 nm laser excitation wavelength. The laser power on the sample was low enough (1 mW) to avoid laser induced modifications during measurements.

In order to evaluate the specific surface area of a representative PLD sample annealed at 500 °C, a deposition at 5 Pa O_2 on a large area Al foil (corresponding to a deposited mass of several mg) was also performed. The surface area was determined by N_2 adsorption–desorption at -196 °C with the BET method using a Micromeritics TriStar 3000 instrument.

TNT photoanode was also characterized by SEM and Raman spectroscopy.

Electrochemical and photoelectrochemical characterization

All the electrochemical and photoelectrochemical experiments were performed in a three-electrode cell in which a Ti/TiO_2 photo-anode (working area of 1 cm^2) was used as the working electrode, a platinum grid as the counter electrode, and a saturated calomel electrode (SCE) as the reference: all the values of potential in the text are referred to SCE.

Depending on the runs, irradiation of the samples was guaranteed by a 300-W Xe lamp (Lot Oriel) equipped with suitable filters to select the right wavelength, or by a tungsten filament and a high-pressure UV-vis lamp (Osram Ultra-Vitalux, 300 W) with a main emission line in the UV region near 360 nm [41-43]. The average UVA/UVB (280-400 nm) power light density, striking on the electrodes surface, was measured by a light meter HD2302.0 (Delta OHM); average values in the range from 1000 and 1350 μW cm^{-2} were measured, depending on the relative position of the sample, with respect to the light source.

Cyclic voltammetry (CV) and Electrochemical Impedance Spectroscopy (EIS) measurements were performed for PLD samples deposited at 3, 5 and 10 Pa annealed at 500°C with constant deposited mass per unit surface (0.5M), in order to investigate the effect of their different morphology on the mechanism of charge transfer at the semi-conductor/electrolyte interphase. EIS measurements were performed in KOH 0.1M solutions in a frequency range from

100 kHz to 0.1 Hz with a frequency response analyzer (FRA, Model 7200 AMEL) coupled with a potentiostat (AMEL 7050). The runs were conducted both in the dark and under illumination at 365nm wavelength.. EIS data were quantitatively interpreted by the equivalent circuit approach. Zassist and ZSimpWin software packages were used to perform impedance experiments and data manipulation, respectively.

CV measurements were performed without illumination in a nominal range of potential from 0.4V to -1,4 V, in (0.1M) ferro/ferricyanide solution, i.e. a well-known reversible redox couple which is generally used to gain information on the charge transfer process at solid/solution interfaces.

The PEC water splitting behaviour of all the PLD films was investigated in aqueous KOH solution (0.1 M). For comparison purpose, the same experiment was performed over the TiO_2 nanotube layer photoanode.

The performance of the TiO_2 photo-anodes was evaluated by measuring the photocurrents produced under an external bias [15-17, 44-46], provided by a potentiostat (Amel 7050). Polarization curves (potential ramps from -0.8 V to about 0.5 V, with a scan rate of 5 mV s^{-1}) were used to compare the performance of different samples.

PEC experiments were also performed with an aqueous KOH solution (0.1 M) in the presence of ethanol (Carlo Erba, 99.9%), ethylene glycol (Sigma-Aldrich, 99.8%) or glycerol (Sigma-Aldrich, >99%) by varying their volume fraction in the 2-40% range.

Results and discussion

Photoanode structure and morphology

The morphology of *as deposited* (as grown) TiO_2 films obtained by PLD at room temperature at different oxygen background pressures (keeping constant the total deposited mass per unit surface (0.5*M*)) is shown in the SEM images of Figure 1 a-d (i.e. 3, 5, 10 and 15 Pa, respectively). Moving from 3 Pa to 15 Pa of oxygen, the effect of increasing the spatial confinement of the plasma plume by the surrounding gas is evident in an increase of porosity, as discussed in previous works [34, 47]. In fact, the gas pressure favours nucleation of the ablated species in the gas phase, leading to the formation of clusters which are subsequently slowed down upon diffusion in the background gas. This allows the tuning of the growth mechanisms from atom-by-atom deposition in vacuum towards low kinetic energy, forward directed cluster assembling at higher gas pressure, with a corresponding gradual variation of film morphology from compact and dense to a columnar structure, and eventually to a nanoporous quasi-1D, vertically oriented assembly. Indeed, as shown in Figure 1 (as deposited films), the above-mentioned parameters were optimized to grow a compact and dense film at 3 Pa O_2, which evolves when increasing pressures are considered. Starting from 5 Pa O_2, a vertically oriented, columnar-like nanostructure, is obtained; at pressures higher than 10 Pa, it clearly evolves into hierarchical structure resembling a forest of nano-trees [33]. Fine nanoparticles (about 10 nm in size) are observed, which are

organized at a multi-scale level, from the single nanoparticle (~10 nm scale) to the branches (~100 nm scale) up to the entire structure (micron-scale). The insert of Figure 1B shows a magnification of the structures obtained at 5 Pa, highlighting the fine structure at the nanoscale, and the hierarchical organization of fine nanoparticles into quasi vertical mesostructures.

By varying the oxygen pressure in the 5-15 Pa range the shape and packing of the quasi-1D structures are thus tuned, and, as a result of the different growth mechanisms, film density and porosity are thus strongly related to the background gas pressure. Figure 2 (dashed black line) shows the variation of film density as a function of the oxygen partial pressure: as expected, moving from 3 to 15 Pa O_2 pressure, the density decreases from 3.2 g cm^{-3} to about 0.5 g cm^{-3}. The corresponding estimated porosity is also shown in Figure 2 (solid red line): in line with the density decrease, the film porosity increases from 18% at 3 Pa O_2 to about 85% at 15 Pa O_2.

SEM images in Figure 1 also provide the film thickness for the 0.5*M* samples, which increases from about 500 nm to more than 3 µm when moving from 3 Pa to 15 Pa deposition pressure. The effect of different thickness was then addressed for films grown at 5 Pa O_2 by varying the mass per unit surface in the 0.5*M*-2*M* range. SEM images (not shown) point out that moving from mass 0.5*M* to mass 2*M* film thickness increases from about 900 nm to about 3600 nm, respectively; however, the overall morphology is not significantly affected by the variation of the mass of deposited material.

To investigate the effect of the post-deposition thermal treatments on samples morphology, SEM analyses were accomplished on the samples annealed at 500 °C, 650 °C and 800 °C. Figure 3 shows SEM images of TiO_2 films deposited at 5 Pa and 10 Pa O_2 after annealing at different temperatures, and compared to the as-deposited materials. For films grown at 5 Pa, the sintering effect at 500 °C and 650 °C results in vertically oriented nanostructures, while when the annealing temperature is elevated up to 800 °C a strong coalescence within the structures is observed, leading to a marked decrease in nanoscale porosity. In the case of the films deposited at 10 Pa, inspection of Figure 3 points out that the post-deposition thermal treatment in air at 500 °C or 650 °C does not change the overall morphology of the more open, tree-like structures grown at this pressure: thermal treatments mainly affect the shape of single nanoparticles and the size, that results slightly increased by higher annealing temperatures. Also, a change in their mutual degree of connectivity is visible, with an increased coalescence among particles (sintering effect). Conversely, for the sample annealed at 800 °C a marked coalescence effect is observed, although to a lesser extent than what detected for the sample grown at 5 Pa.

The crystalline structure of the films was characterized by Raman spectroscopy, which is sensitive to the local crystalline order/disorder and provides a fingerprint of the TiO_2 crystalline phase (anatase/rutile) [48]. In figure 4 Raman spectra of the film grown at 5 Pa O_2, representative of a more compact morphology, and Raman spectra of the

film grown at 10 Pa O_2, with a more open morphology, are reported, both for as deposited film and after annealing at 500, 650 and 800°C. The spectra of the as deposited films are characterized by two large bands, which are fingerprints of a highly disordered and almost amorphous structure due to the room temperature growth process. Conversely, as expected, high temperature annealing in air induces transition to a crystalline structure. As a result of the thermal treatment, at all the explored temperatures the dominant TiO_2 crystalline phase of the film grown at 5 Pa O2 (left panel of figure 4) is anatase, as evidenced by the presence of narrow peaks at 144, 197, 399, 519 and 639 cm^{-1} (another expected anatase peak at 519 cm^{-1} is hidden by the intense peak at 521 cm^{-1} of the silicon substrate) [48]. The same behaviour is observed for the sample grown at 3 Pa (spectra not reported).

Moving to films deposited at higher pressures (10 Pa , spectra on the right panel of the figure 4, and 15 Pa, not reported) peaks at 443 cm^{-1} and 610 cm^{-1}, corresponding to the rutile phase, start to appear together with the anatase peaks after annealing at 500 °C. The relative intensity of these to peaks with respect to the anatase peaks increases with increasing annealing temperature. From this parameter it is possible to estimate the rutile content [48] that results within 20% for annealing at 500 °C, in agreement with previous results [34], and it increases up to 50 % for the 15 Pa sample at higher temperatures. Such observed structural features, and, in particular, the oxide phase evolution upon annealing, is in agreement with previous [34] Raman characterizations of TiO_2 films grown under similar experimental conditions. In the same work [34] XRD measurements confirmed this evolution of the crystalline structure for which an average domain size in the range 10-20 nm was estimated from the width of XRD reflections. Of note, in line with previous results [34] the crystalline structure of PLD films annealed at 500°C is fully comparable with those annealed at 400°C , i.e. the same annealing temperature of the nanotubolar TiO_2 sample (see below).

Figures 5a and 5b show SEM images of the annealed TNT photoanode (top view and cross-view, respectively). Nanotubes were found to have an outer diameter of approximately 80-90 nm and a length of about 700 nm. Figure 4 shows the Raman analysis (spectrum c) indicating that also in this case the dominant TiO_2 crystalline phase is anatase.

Electrochemical response

EIS and CV measurements in the dark were performed to investigate the electrochemical behavior of the TiO_2 nanostructures prepared by PLD. Samples deposited in the 3-10 Pa O_2 pressure range (i.e. ranging from compact to vertically oriented or hierarchical nanostructures) with constant deposited mass per unit surface (0.5*M)* and annealed at 500°C were investigated, in order to gain information on the electrochemical properties and transport phenomena, with particular reference to the different films morphology (i.e. porosity and thickness). Of note, both EIS and CV measurements were performed at negative applied potentials, since no charge transfer is expected in the dark, at oxidative potentials, according to the nature of the TiO_2-based photoanodes (i.e. n-type semiconductors).

The results of EIS measurements performed in the dark at -0.7 V are reported in Figure 6, in terms of Nyquist plots.

Data were quantitatively interpreted by means of the equivalent circuit approach. Among the several equivalent circuits that have been proposed in the literature in order to represent the processes involved at the interphase electrode/electrolyte of porous structures, a quite simple circuit was successfully applied in the present case, where an element that accounts for the resistance of the solution (*Rs*), is connected in series with three capacitor/resistance elements [$R_s(C_1R_1)(C_2R_2)C_3R_3$)]. Solid lines in Figure 6 refer to the model fits, while Table 1 resumes the values of the circuital parameters calculated by the fit of experimental data. Of note, the solution resistance (*Rs*) is not reported since in all cases it was found very low, due to the high conductivity of the solution. Depending on the case, constant phase elements are used instead of pure capacitors, for a better agreement with experimental data: their admittance is expressed by $Y = Q(j\omega)^n$, being $n = 1$ for perfect capacitors. The values of time constant ($\tau = (RQ)^{1/n}$), are also reported in Table 1; actually, the analysis of the time constants τ, can be useful for the interpretation of the circuit, and hence of the occurring processes. If data in Table 1 are compared, slight differences among the parameters related to the first element R_1C_1, which is associated to the high frequency range, are observed for the samples obtained at different pressures, being the one at 10Pa, that with the higher conductivity. However, values of time constants calculated for the three samples are almost of the same order, indicating very similar rate of the processes involved at highest frequency. In particular, the low values obtained for the τ_1 constants (i.e. order of microseconds) can be attributable to phenomena of charges adjustment occurring in the solid bulk.

Greater differences are observable between the responses of the three samples, at lower frequency. The related arc may be considered as the convolution of two semicircles, associated to two slower processes (τ_2 in the order of s and τ_3 in the order of ms, respectively), which may indicate diffusive and reactive processes. In particular, the values of the exponent n_2 quite lower than 1, can be related to possible presence of diffusive effects in the porous structure of the electrode (n=0.5 should correspond to a Warburg impedance). Besides, the cathodic reaction can be reasonably represented by the R_3C_3 element.

The above interpretation is in agreement with the morphology of the samples. In particular, the sample deposited at the lowest pressure value, 3 Pa, i.e. dense and non-porous TiO_2 film, shows the highest diffusive limitation (i.e. high value of R_2 and τ_2). Conversely, lower values for R_2 and τ_2, are measured at the sample deposited at 5 Pa, where higher porosity is obtained. However, this effect is maintained only when the regular structure is obtained (a columnar-like structure has been revealed at 5 Pa sample). Actually, low resistance to the charge transfer (i.e. low value of R_3) is measured for samples at 10 Pa, but the high value of R_2 suggests that high diffusive limitations are again present at this sample, probably becouse the hierarchical, tree-like, morphology which is obtained at this sample.

In fact, previous work [49] was carried out in our lab on similar PLD samples, in which CVs measurements, performed at different potential scan rates, allowed us deriving information on the capacitance and in turn, on the electrochemically active surface of the samples. Of note, samples deposited at high pressures (i.e. 10 Pa) showed the highest value of global capacitance, but a lower value for the ratio between external and global capacitance if compared to samples deposited at intermediate pressure (i.e.5 Pa). Accordingly, this indicated that the increasing porosity observed for open tree-like morphologies mainly affects internal porosity leading to negligible interaction with the ions electrolyte.

Dedicated CV experiments in a ferro/ferricyanide solution were performed for samples deposited at 3, 5 and 10 Pa to analyze more in details the effect of the deposition pressure, and hence of films structure/morphology, on the corresponding charge transfer properties. Figure 7 shows a comparison between the trends of the CVs where only the cathodic region is reported. In fact, in all cases no oxidative peaks were observed as typical for n-type photoanodes under dark conditions (see inset). The results clearly show that samples deposited at 5 and 10 Pa are by far more active than that deposited at 3 Pa. In particular, the higher current measured at the cathodic peak for sample deposited at 10 Pa confirms its superior conductive properties. Besides, the shift at more negative potential observed for its cathodic peak indicates a slightly lower activity if compared with sample deposited at 5Pa.

Photoelectrochemical response

To assess the functionality of the TiO_2 nanostructures prepared by PLD in view of water splitting applications we investigated the behavior of so prepared films as photoanodes in a photoelectrochemical cell in 0.1M KOH solution, analyzing the effects of different background pressures, deposited mass, and annealing temperatures. The PEC performances are shown in Figures 8 for PLD samples grown at 5, 3, 10 and 15 Pa O_2 (Fig. 8a, 8b, 8c and 8d, respectively). The results obtained in the case of TNT photoanode are reported in Figure 6b for comparison purpose.

In order to compare the performances of different film morphologies, the photoelectrochemical behaviour of TiO_2 films grown at different pressures was first investigated, keeping the total deposited mass per unit surface of the photoactive material constant ($0.5M$) as well as the annealing temperature (i.e. 500°C). All the amorphous as deposited samples showed negligible photoresponse (not reported) due to the presence of a high number of defects which can act as traps and recombination centers for the photogenerated charge carriers. Instead, a significant enhancement in photoresponse was observed for annealed samples and the trends of the polarization curves obtained under light irradiation may be used to compare the different photoactivity of the samples. A typical example of polarization curves, both in the dark and under illumination, is depicted in Figure 8a for the sample deposited at 5 Pa and annealed at 500 °C (see curves a

and b, respectively). As expected, under dark conditions negligible photocurrent is observed (less than 3 μA cm^{-2}), over the whole investigated potential range, indicating that no reaction occurred at the photoanodes in the absence of light illumination. On the contrary, upon illumination photocurrent evolution is observed starting at approximately -0.8 V (photopotential onset), as a result of the charge carriers (i.e. electron-holes pairs) generation from the incident light and the subsequent water oxidation occurring at the photoanodes by holes. An almost linear dependence of the photocurrent density on the potential is observed in the first part of the curve, because of the efficient charge carrier separation, under the effect of the applied bias [50-52]. Then, after a certain value *V**, a decrease of slope is generally measured, and finally a saturation condition is reached, where the effect of the applied potential becomes not more significant. Analogous trends of polarization curves, were obtained at the other samples: however, depending on the sample, different values of photopotential onset, saturation current density, and *V**, were measured. Thus, in order to make a quantitative comparison between the performances of the different samples, the photopotential onset values and the photocurent density measured at a fixed potential are firstly considered. The third parameter, *V**, is then taken into account when the photoconversion efficiency is evaluated, as reported in the following.

The effect of the oxygen deposition pressure (and in turn of the morphology) on the photoresponses can be observed by comparing curve *a* in Figure 8a (i.e. film deposited at 5Pa) with curves *a* in Figures 8b, 8c and 8d (i.e. films deposited at 3, 10 and 15 Pa, respectively). For sake of clarity, the effect of the oxygen deposition pressure is evidenced in Figure 9, where the photopotential onset, and the steady-state photocurrent density recorded at 0.5 V (Figure 9a and 9b, respectively), are reported for samples annealed at 500°C. Data refer to samples with constant deposited mass per unit surface (0.5*M*), but also data referring to sample with *M* and 2*M* are included in the same graph for comparison.

Of note, the strongest negative effect on the performance of the photoanodes seems to be correlated to the porosity increase corresponding to the highest deposition pressure values. As a matter of fact, for samples deposited at the highest oxygen pressures (i.e. 10 and 15 Pa) the photopotential onset is shifted considerably to less negative values (i.e. near -0.7 V), and the photocurrent density is significantly lower than that for the samples at lower pressure, approaching values close to 15 μA cm^{-2}. This suggests a less efficient generation and transfer of photogenerated charge carriers and higher recombination losses, as well [53-55]. If the most performing samples are compared, a photopotential onset of about -0.75 V is measured for the sample deposited at 3 Pa (i.e. compact and dense film), which is less negative than that of samples deposited at 5 Pa (i.e. -0.8 V). Lower photocurrent density is correspondingly measured for sample at 3 Pa (i.e. 55 μA cm^{-2} vs. 65 μA cm^{-2}).

Figure 10 a and 10b depict the results of EIS measurements carried out under 365 nm wavelenght irradiation, at 0.5V of bias potential. The resulting spectra are reported in Figure 10a and 10b in terms of Bode and Nyquist plots, respectively,

for samples deposited ad 3, 5 and 10 Pa. The quantitative analysis of data has been done using the equivalent circuit approach with the same electrical circuit used for the EIS measurement performed in the dark (see above). Table 2 resumes the values of the fitting circuital parameters. Also in this case, the circuit elements associated to the high and medium frequencies could be attributable to the response of the bulk structure, and to possible diffusion effects, respectively. Besides, the third circuit element, associated to the lowest frequency range, may be related to the transfer of photogenerated holes toward the electrolyte. As it can be observed, the data related to the sample deposited at 10 Pa justify the low photoresponse obtained at this sample. As a matter of fact, the value of τ_3, higher than that related to the samples obtained at the lowest pressures, confirms the slow charge transfer at this sample. Moreover, the high value of τ_2 indicates that also diffusive processes could negatively affect the whole photocatalytic process at this sample.

If the samples deposited at lower pressures are considered (i.e. 3 and 5 Pa), the higher photoresponse observed for the sample deposited at 5 Pa can be explained in view of a combined effect of both diffusive and charge transfer processes. Accordingly, by comparing τ_2 and τ_3, the vertical oriented structure is expected to favor the accessibility by ions electrolyte which compensates for the slow charge transfer.

In order to make a more exhaustive comparison, also the photoconversion efficiency (η%) has been evaluated. In electrically driven photo-processes, as in this case, equation (1) can be properly used [56,57] as it takes into account not only the light power, but also the applied external potential:

$$\eta\ (\%) = \frac{J\,(E^{\circ} - |E\mathrm{app}|)}{I} * 100 \qquad (1)$$

where, J is the photocurrent density (μA cm^{-2}), E°=1.23V is the standard reversible potential for water splitting, $|E_{app}|$ is the applied potential evaluated as the difference between the bias potential and the OCV under the irradiated power light, and I is the UV incident light power density. Of note, dedicated experiments [49] performed at selected wavelengths, indicated the negligible contribution of the visible-light on the total activity of the investigated samples which is in line with previous work showing that the optical gap for PLD hierarchical TiO_2 deposited under O_2 atmosphere and annealed in air at 500 °C is about 3.2-3.3 eV [34], i.e. about 370-390 nm, without any detectable trend with respect to deposition pressure.

Figure 11a shows the variation of η% as a function of the applied potential. As typical [56,57], voltage-dependent trends can be observed: initially the efficiency increases with the increasing applied potential reaching a maximum, where the electron-hole separation is superior under the effect of the applied bias, and then begins to decrease at higher applied

bias, where the external electrical work, done to separate the charges, negatively affects the overall photoconversion efficiency. It must be observed that the maximum in this curve is obtained at a potential value about corresponding to the *V** in the polarization curve (see Figure 8a) which can be individuated as the optimal working potential, at which the photoelectrochemical water splitting process could be carried out.

On these bases, the sample deposited at 5 Pa results the best performing, not only because it achieves the highest maximum efficiency of ca. 4%, but also because this efficiency is obtained at very low bias (near -0.6 V). Conversely, the sample deposited at 3 Pa and those deposited at 10-15 Pa show lower values of maximum efficiencies, of ca. 2.0% and 0.5%, respectively, which are obtained at higher potential.

On the basis of the above results, the effect of film thickness, on the photoresponses was further investigated for samples deposited at 5 Pa (i.e. for the morphology that had shown the best performances) by varying the mass of deposited material in the 0.5*M*-2*M* range. All the investigated samples were annealed at the same temperature (i.e. 500 °C).

As it clearly appears from Figures 9a the photopotential onset is approximately the same (i.e. near -0.8 V) for all the samples deposited at 5 Pa; however, a clear effect of film thickness on the photoresponse is apparent from Figure 9b, and moving from sample-0.5*M* to sample-*M* (i.e. from ca. 900 nm to ca. 1400 nm of thickness) the photocurrent is remarkably improved. In particular, sample-*M* yields a photocurrent density of roughly 130 μA cm^{-2} at 0.5 V, which represents ca. a 2-fold increase of the photocurrent response if compared to sample-0.5*M*. Besides, the further increase of the thickness up to 3600 nm (sample-2*M*) results in a photoresponse decrease, so that a photocurrent density comparable to that of sample-0.5*M* is attained. This outcome suggests the existence of an optimal thickness value for the quasi 1D structures, which can guarantee improved photoactivity. This is clearly shown by the corresponding photoconversion efficiencies, plotted in Figure 11b. As a matter of fact, the maximum photoconversion efficiency of the sample-*M* is increased to ca. 6.3% (vs. 4 and 3.7%, for sample-0.5*M* and sample-*M*, respectively). Such a behaviour seems peculiar of quasi 1D structures. Indeed, the effect of the variation of thickness was further investigated for samples deposited at 3 Pa that are conventional thin films (i.e. compact and dense). Of note, in this case we observe that photocurrents results (see Figures 8b, 9a and 9b) and the corresponding photoconversion efficiencies data (Figure 11c), show a negligible effect on the photoactivity in the whole potential range when moving from sample-0.5*M* to sample-*M* (i.e. from about 500 nm to about 1500 nm of thickness).

For comparison purpose, in Figure 11b, the results obtained for the TNT photoanode are also reported. Of note, in this case, the photoconversion efficiencies are very similar to those calculated for sample-0.5*M* which is in line with their comparable thickness. However, in the case of the TNT photoanode the maximum efficiency is obtained with an applied potential which is higher than that for the PLD sample.

Furthermore, in order to investigate the effect of the post-thermal treatment (and thus of crystallinity) on the photoelectrochemical performances, additional tests were performed over TiO_2 photoanodes prepared at different background pressures and annealed at 650 °C. For comparison the same mass (i.e. 0.5*M*) was deposited in this case. The photoelectrochemical results are shown, in terms of photocurrent density generated at 0.5 V and photocurrent efficiency, in Figures 12 (see white bars) and 11d, respectively.

In line with the results obtained in the case of samples annealed at 500 °C, also for samples annealed at 650 °C the best performances are associated with the sample deposited at 5 Pa oxygen. In fact, as shown in Figure 12, the sample deposited at 5 Pa oxygen shows the highest photocurrent densities reaching a value of 200 μA cm^{-2} at 0.5 V which represents ca. a 4-fold increase of the photocurrent response if compared to all the other samples. Accordingly, the sample deposited at 5 Pa oxygen exhibits conversion efficiencies as high as 8% (see Figure 11d), which are highly enhanced as compared to the other investigated samples. Indeed, great care must be paid in evaluating the existing literature photoconversion efficiency results [3] because the use of very different experimental conditions (e.g. light source and energy, photo-anode preparing conditions, electrolyte nature and concentration) prevents us from a direct and exhaustive comparison. However, such a value of photoconversion efficiency is quite comparable to those typically obtained over other TiO_2 based photoanodes under UV irradiation [15, 58, 59].

The clear effect of the post-thermal treatment on the photocatalytic performances can be observed, by comparing Figures 9b and 12, i.e. considering samples deposited at the same pressure but annealed at 500 and 650 °C, respectively. Except in the case of the sample deposited at 3 Pa oxygen, upon increasing the annealing temperature from 500 to 650 °C, the photocatalytic activity considerably increases. As a matter of fact, the photoresponse of samples deposited in the 5-15 Pa oxygen range is almost trebled, whereas it was very similar for samples deposited at 3 Pa.

Of note, the photo-electrochemical response of samples annealed at 800 °C was also investigated and representative results are reported in Figure 12 for samples deposited at 5, 10 and 15 Pa (i.e. see black bars). Extremely low activity was found in this case. As a matter of fact very low values of photocurrent density (i.e. close to 10 μA cm^{-2} at 0.5 V) were measured.

Finally, photoelectrochemical tests were also carried out in the presence of ethanol, ethylene glycol or glycerol. For this purpose, the behaviour of the sample prepared at 5 Pa of oxygen (i.e. for the morphology that had shown the best performances) and annealed at 500 °C (mass = *M*) was investigated. Figure 13 shows the results in terms of the parameter γ evaluated as ratio between the photocurrent values obtained at 0.5 V with and without the organics as a function of their volume fraction. Accordingly, when $\gamma > 1$, it accounts for the performance gain due to the presence of the organic compounds.

As it clearly appears from Figure 13, all the investigated organic compounds improves the PEC performances which is mainly attributed to the great increase of charge separation efficiency since they act as sacrificial electron donor by consuming photogenerated holes and/or oxygen, thus lowering the electron-hole recombination and/or H_2–O_2 back reaction, i.e. the most important reactions for decreasing the light-to hydrogen conversion efficiency [60]. According to several literature reports [61-64] the photo performances gain using ethanol as scavenger is the lowest if compared to ethylene glycol and glycerol because of the different chemico-physical properties of the alcohols (e.g. number of α-H and OH groups, the proportion between carbon and hydroxyl groups number, alcohol polarity and their standard oxidation potentials). However, specific optimum concentration values were found for each organic compound. In the case of ethanol the increase of photo response is evident at the lowest investigated concentration (i.e. 5 vol.%) and then, according to the literature [65, 66] it stabilizes at higher concentrations. The same saturation effect is observed in the case of ethylene glycol. Besides, in the case of glycerol, the highest performances are obtained with very low concentrations of the sacrificial agent (i.e. 2 and 3 vol.%) while further concentration increase has adverse effect resulting in a photoresponse even lower (i.e. $\gamma < 1$) than the pure KOH solution. This may be explained considering that the solution becames very viscous which is exepected to negatively affect light penetration and/or electrolyte ions transport/diffusion.

The bulk of the above results reveals a strong dependence of the photoelectrochemical performances on samples structure, morphology and multiscale organization, as well. A tentative explanation for the observed trends in photocurrent performances as a function of deposition pressure and annealing treatment can be proposed, in relation to the accessible active surface (depending on total surface area and thus on nanoscale porosity), carrier recombination (affected by degree of crystallinity and grain boundaries) and electrical transport (which is expected to depend on the film connectivity, vertical or quasi-1D morphology and crystallinity). As for morphology, we found that 5 Pa deposition pressure corresponds to an optimum condition for the film performance. More in particular, for samples annealed at 500°C, the photocurrent response was found to increase by moving from 3 to 5 Pa O_2 pressure, whereas there was a drastic decrease in performance associated with the samples deposited at higher O_2 pressures, i.e. 10 and 15 Pa O_2. This trend can be ascribed to the peculiar morphology of PLD grown samples in the 3-15 Pa range. As previously discussed, the deposition background gas pressure strongly affects the TiO_2 film growth mechanisms and its final porosity. In fact, while at the lowest pressure (i.e. 3 Pa) a 500 nm thick, dense and compact film develops, the increasing deposition pressure in the 5-15 Pa range allows a vertically oriented, quasi-1D organization (from a columnar-like to a hierarchical tree-like nanostructure) with structures reaching more than 1μm in length. As a consequence, since the same mass was deposited for each sample, the increasing deposition pressure leads to a parallel decrease in film density, i.e. to an

increase in film porosity and thus in the available active surface area. On this regard, it was found that the BET specific surface area of films deposited at 5 Pa O_2 after thermal treatment at 500 °C was around 25 m^2 g^{-1}, with a pore size distribution in the range from a few nm to ~100 nm. This surface area value is representative also of films annealed at 650 °C, since SEM shows that no significant change in morphology occurs at this temperature, while annealing at 800 °C results in a strong coalescence and, presumably, in a strong decrease of the available surface.

In a previous work [32], it was shown that, as the deposition pressure increases, specific surface area increases while density decreases, so that the *roughness factor*, i.e. the ratio between the available material surface and the geometrical footprint of the film, has an optimum value for intermediate pressure conditions. In our case, by knowing film density, thickness and specific surface, it is possible to evaluate the roughness factor: in the case of films deposited at 5 Pa we calculated a *roughness factor* per unit thickness around 50 μm^{-1} (i.e. 50 cm^2 of active surface for a film 1 μm thick and with a footprint of 1 cm^2).

On this basis, it is not surprising that samples deposited at 3 Pa O_2 show a lower photoactivity. In fact, in order to achieve high photoelectrochemical performances, a large surface area is desired along with suitable electronic features (e.g. adequate band edge positions and rapid charge separation properties): however, in the case of sample deposited at 3 Pa O_2 a compact TiO_2 film is obtained with small porosity (18%) and thus low surface area. Conversely, the enhanced performances observed for the sample deposited at 5 Pa O_2 could be reasonably ascribed to the larger surface area which entails the availability of an increased number active sites for the reaction. Moreover, it may be argued that a more open structure with vertical void channels, typical of quasi-1D nanomorphologies obtained with the increased deposition pressure, can offer the advantage of better electrolyte ions transport/diffusion allowing the whole surface to be active in the photoelectrochemical process. This was confirmed by CV and EIS results, where both the accessibility of the active sites by the electrolyte ions and the high charge transfer capacity were indicated as beneficial in determining the high performances of sample deposited at intermediate pressure (i.e. 5 Pa).

On the other hand, the significant photoresponse decrease observed for samples deposited at the highest deposition pressures (i.e. 10 and 15 Pa O_2) could be tentatively ascribed to the higher recombination losses as a consequence of the excessive thickness and more open morphology of tree-like structures, i.e. lack of connectivity (see the discussion below). In addition, according to CV and EIS measurements, both slow charge transfer properties and diffusive limitations may explain the low photoelectrochemical response observed for samples deposited at high temperatures. Besides, possible effect of the different crystalline structure (a mixture of anatase/rutile for sample deposited at 10 and 15 Pa O_2) could not be completely ruled out even though it sounds unlikely. In fact several works reported that mixtures of anatase/rutile are more active than pure rutile or anatase in photocatalytic reactions since the anatase/rutile phase junction is supposed to improve charge carriers separation and their life-time. [67-70]

Once the structure/morphology of the material has been optimized, it was found that the increase of the film thickness does not correspond to a monotonic increase in the photocurrent, even though, of course, the total surface area increases. Possible explanations for this behaviour include non-optimized carrier transport for very high thicknesses. In addition, several reports focused on nanotubular TiO_2 photoanodes [71-74] or other TiO_2 nanostructures [20,75], reported the existence of a critical thickness value which has been explained as a result of an optimum balance between light absorption and charge carriers life-time. Accordingly, for films with low thickness as in the case of mass-0.5*M* sample, the amount of the material is likely too low and the light absorption too weak as well, thus leading to low efficiencies. Otherwise, for films with too high thickness, as in the case of mass-2*M* sample, the long transport distance for charge carriers may lead to undesirable recombination phenomena. In addition, mass-transport limitations at the electrode/electrolyte interphase could be invoked to explain the inefficiencies observed for the longer hierarchical treelike structures, e.g. leading to a minor electrolyte ions infiltration and limiting the true active surface only to the top part of the film.

Concerning the effect of thermal treatments, the increased photoelectrochemical performances observed for samples annealed at 650 °C can be related to the efficient sintering between nanoparticles, that can reduce amorphous regions or grain boundaries and consequently can ensure a slightly higher degree of cristallinity. This likely improves conductivity and charge transport and also favours a probable defect healing (e.g. at grain boundaries) which may reduce carrier recombination. On the contrary, for films annealed at 800 °C the reduction in active surface, resulting from the strong degree of coalescence, probably plays a major role, resulting in a negligible photocurrent.

As a final point, the photoresponse was further strengthened with the presence of organic sacrificial reagents who served as hole scavengers. In particular, the performance gain observed in the presence of very low amounts of glycerol is particularly attractive. In fact, glycerol is the major byproduct of biodiesel production and its photoelectrochemical re-utilization is of great industrial interest in order to improve the global biodiesel economy [76, 77].

Conclusions

Quasi-1D and tree-like hierarchical nanostructured TiO_2 films were prepared by Pulsed Laser Deposition (PLD) and evaluated as potential photoanodes for the photoelectrochemical (PEC) water splitting reaction.

In particular, the photoelectrochemical responses have been discussed as a function of the different material morphologies and structures, which were tailored by varying the preparation conditions.

At first, samples were prepared by changing the oxygen pressure (in the range 3-15 Pa): it was found that film growth can be tuned at the nanoscale from compact/dense films to columnar/vertically oriented or hierarchical porous nanostructures. In relation to optimized values of density/surface area, crystallinity and electron transport, the best

photoelectrochemical performances were associated with the sample prepared using 5 Pa of oxygen. In particular, according to CV and EIS analysis, performed both in the dark and under illumination, its accessibility by the electrolyte ions and its charge transfer capacity were indicated as crucial in determining its high photoresponse.

The effect of the variation in the mass of deposited material, that leads to an increased thickness of the catalytic layers, suggested the existence of an optimal thickness value that likely improves the electron transfer. Of note PLD samples showed a photo-activity even higher (i.e. depending on thickness) than TiO_2 nanotubular arrays prepared by anodic oxidation, but presented a lower value of V^* at which the maximum electrical yield may be reached.

The study of the effect of the annealing temperature showed that the photoelectrochemical response increases for samples annealed at 650 °C, indicating the importance of crystallinity and structure connectivity.

The set of results indicates that the TiO_2 nanostructures prepared by reactive pulsed laser deposition (PLD) can be considered of practical interest for photoelectrochemical water splitting applications. In particular, open morphologies characterized by relevant nanoscale porosity and by a vertically oriented morphology have shown promising results achieving photocurrent efficiencies up to 8%, under UV irradiation.

Conversely, tree-like nanostructures (i.e. more open morphologies prepared at 10 and 15 Pa O_2) showed lower PEC water splitting activities, possibly due to the occurrence of higher recombination losses as a consequence of their excessive thickness.

Eventually, the use of organic sacrificial reagents (i.e. ethanol, ethylene glycol or glycerol) has been proved to be exploitable to improve PLD photoanodes performances.

Further optimization of the material structure-morphology, and possible routes for enhancing the response to visible light (e.g. doping, sensitization) offer future opportunities for improving PEC water splitting devices based on nanostructured TiO_2 films prepared by Pulsed Laser Deposition.

Acknowledgements

The authors wish to thank G. D'Ambrosio, for participating to the experimental measurements and to acknowledge the FARB project of the Dept. of Energy, Politecnico di Milano for financial support.

References

[1] Turner J, Sverdrup G, Mann MK, Maness PC, Kroposki B, Ghirardi M, Evans RJ, Blake D (2008) Int J Energ Res 32:379-407

[2] Ball M, Wietschel M (2009) Int J Hydrogen Energy 34:615-627

[3] Bak T, Nowotny J, Rekas M, Sorrell CC(2002) Int J Hydrogen Energy 27: 991-1022

[4] Matsuoka M, Kitano M, Takeuchi M, Tsujimaru K, Anpo M, Thomas JM (2007) Catal Today 122:51-61

[5] Kudo A, Miseki Y (2009) Chem Soc Rev 38: 253-278

[6] Navarro RM, Sánchez-Sánchez MC, Alvarez-Galvan MC, del Valle F, Fierro JLG (2009) Energ Environ Sci 2:35-54

[7] Fujishima A, Honda K (1972) Nature 238:37-38

[8] Fujishima A, Rao TN, Tryk DA (2001) J Photochem Photobiol C 1:1-21

[9] Fujishima A, Zhang X, Tryk DA (2008) Surf Sci Rep 63:515-582

[10] Ni M, Leung MKH, Leung DYC, Sumathy K (2007) Renew Sust Energ Rev 11:401-425

[11] Anpo M, Takeuchi M (2003) J Catal 216:505-516

[12] Kitano M, Tsujimaru K, Anpo M (2008) Top Catal 49:4-17

[13] Chen J, Yang D, Song D, Jiang J, Ma A, Hu MZ, Ni C(2015) J Power Sources 280:649-666

[14] Lin Y, Yuan G, Liu R, Zhou S, Sheehan SW, Wang D (2011) Chem Phys Lett 507:209-215

[15] Palmas S, Polcaro AM, Rodriguez Ruiz J, Da Pozzo A, Mascia M, Vacca A (2010) Int J Hydrogen Energy 35: 6561-6570

[16] Palmas S, Da Pozzo A, Mascia M, Vacca A, Matarrese R, Nova I (2012) J Appl Electrochem 42:745-751

[17] Palmas S, Da Pozzo A, Delogu F, Mascia M, Vacca A, Guisbiers G (2012) J Power Sources 204:265-272

[18] Wolcott A, Smith WA, Kuykendall TR, Zhao Y, Zhang JZ (2009) Small 5:104-111

[19] Bang JH, Kamat PV (2010) Adv Funct Mater 20:1970-1976

[20] Su Y, Lee M, Wang G, Shih Y (2014) Chem Eng J 253:274-280

[21] Feng X, Shankar K, Varghese OK, Paulose M, Latempa TJ, Grimes C A (2008) Nano Lett 8:3781-3786.

[22] Liu M, de Leon Snapp N, Park H (2011) Chem Sci 2:80-87

[23] Sánchez-Tovar R, Lee K, García-Antón J, Schmuki P (2013) ECS Electrochem Lett 2:H9-H11

[24] Sánchez-Tovar R, Fernández-Domene RM, García-García DM, García-Antón J (2015) J Power Sources 286:224-231

[25] Mor GK, Varghese OK, Paulose M, Shankar K, Grimes CA (2006) Sol Energ Mat Sol C 90:2011-2075.

[26] Shankar K, Basham JI, Allam NK, Varghese OK, Mor GK, Feng X, Paulose M, Seabold JA, Choi KS, Grimes CA (2009) J Phys Chem C 113:6327-6359

[27] Roy P, Berger S, Schmuki P (2011) Angew Chem Int Ed 50:2904-2939

[28] Paramasivam I, Jha H, Liu N, Schmuki P (2012) Small 8:3073-3103

[29] Kowalski D, Kim D, Schmuki P (2013) Nano Today 8:235-264

[30] Liu N, Chen X, Zhang J, Schwank JW (2014) Catal Today 225:34-51

[31] Sauvage F, Di Fonzo F, Li Bassi A, Casari CS, Russo V, Divitini G, Ducati C, Bottani CE, Comte P, Graetzel M (2010) Nano Lett 10:2562-2567

[32] Passoni L, Ghods F, Docampo P, Abrusci A, Martí-Rujas J, Ghidelli M, Divitini G, Ducati C, Binda M, Guarnera S, Li Bassi A, Casari CS, Snaith HJ, Petrozza A, Di Fonzo F (2013) ACS Nano 7:10023-10031

[33] Casari CS, Li Bassi A (2014) In: Srivastava AK (ed.) Oxide Nanostructures: Growth, Microstructures and Properties, Pan Stanford Publishing, Singapore, pp. 99-114

[34] Di Fonzo F, Casari CS, Russo V, Brunella MF, Li Bassi A, Bottani CE (2009) Nanotechnology 20 (015604): 1-7

[35] Gondoni P, Ghidelli M, Di Fonzo F, Carminati M, Russo V, Li Bassi A, Casari CS (2012) Nanotechnology 23 (365706):1-8

[36] Gondoni P, Ghidelli M, Di Fonzo F, Russo V, Bruno P, Martí-Rujas J, Bottani CE, Li Bassi A, Casari CS (2013) Nanosci Nanotechnol Lett 5:484-486

[37] Matarrese R, Nova I, Li Bassi A, Casari CS, Russo V (2014) Chem Eng Trans 41:313-318

[38] Patsoura A, Kondarides DI, Verykios XE (2007) Catal Today 124:94-102

[39] Lianos P (2011) J Hazard Mater 185:575-590

[40] Palmas S, Da Pozzo A, Mascia M, Vacca A, Ardu A, Matarrese R, Nova I (2011) Int J Hydrogen Energy 36:8894-8901

[41] Zalas M, Laniecki M (2005) Sol Energ Mat Sol C 89:287-296

[42] Hidalgo MC, Maicu M, Navío JA, Colón G (2007) Catal Today 129:43-49

[43] Obregón S, Colón G (2014) Appl Catal B Environ 144:775- 782

[44] Liu J, Yu X, Liu Q, Liu R, Shang X, Zhang S, Li W, Zheng W, Zhang G, Cao H, Gu Z (2014) Appl Catal B Environ 158-159:296-300

[45] Radecka M, Wnuk A, Trenczek-Zajac A, Schneider K, Zakrzewska K (2015) Int J Hydrogen Energy 40:841-851

[46] Gannouni M, Ben Assaker I, Chtourou R (2015) Int J Hydrogen Energy 40:7252-7259

[47] Bailini A, Di Fonzo F, Fusi M, Casari CS, Li Bassi A, Russo V, Baserga A, Bottani CE (2007) Appl Surf Sci 253:8130-8135

[48] Li Bassi A, Cattaneo D, Russo V, Bottani C E, Barborini E, Mazza T, Piseri P, Milani P, Ernst FO, Wegner K, Pratsinis SE (2005) J Appl Phys 98 (074305):1-9

[49] Matarrese R, Palmas S, Nova I, Li Bassi A, Casari C, Russo V, Mascia M, Vacca A (2014) Chem Eng Trans 41:397-402

[50] Zhou B, Schulz M, Lin HY, Shah SI, Qu J, Huang CP (2009) Appl Catal B Environ 92:41-49

[51] Cowan AJ, Tang J, Leng W, Durrant JR, Klug DR (2010) J Phys Chem C 114:4208-4214

[52] Spadavecchia F, Ardizzone S, Cappelletti G, Falciola L, Ceotto M, Lotti D (2013) J Appl Electrochem 43:217-225

[53] Song XM, Wu JM, Tang MZ, Qi B, Yan M (2008) J Phys Chem C 112:19484-19492

[54] Xu Z, Yu J (2011) Nanoscale 3:3138-3144

[55] Zhang K, Shi XJ, Kim JK, Park JH (2012) Phys Chem Chem Phys 14:11119-11124

[56] Khan SUM, Al-Shahry M, Ingler Jr WB (2002) Science 297:2243-2245

[57] Varghese OK, Grimes CA (2008) Sol Energ Mat Sol C 92:374-384

[58] Mor GK, Shankar K, Paulose M, Varghese OK, Grimes CA (2005) Nano Lett 5:191-195

[59] Allam NK, El-Sayed MA (2010) J Phys Chem C 114:12024-12029

[60] Kondarides DI, Daskalaki VM, Patsoura A, Verykios XE (2008) Catal Lett 122:26-32

[61] Bowker M. (2012) Catal Lett 142:923-929

[62] Li Y, Wang B, Liu S, Duan X, Hu Z (2015) Appl Surf Sci 324:736-744

[63] Chen WT, Chan A, Al-Azri ZHN, Dosado AG, Nadeem MA, Sun-Waterhouse D, Idriss H, Waterhous GIN (2015) J Catal 329:499-513

[64] Kumar DP, Reddy NL, Srinivas B, Durgakumari V, Roddatis V, Bondarchuk O, Karthik M, Ikuma Y, Shankar MV (2016) Sol Energy Mater Sol Cells 146:63-71

[65] Strataki N, Antoniadou M, Dracopoulos V, Lianos P (2010) Catal Today 151:53-57

[66] Antoniadou M, Bouras P, Strataki N, Lianos P (2008) Int J Hydrogen Energy 33:8894-8901

[67] Ohno T, Tokieda K, Higashida S, Matsumura M (2003) Appl Catal A: Gen 244: 383-391

[68] Zhang J, Xu Q, Feng Z, Li M, Li C (2008) Angew Chem 120: 1790-1793

[69] Shen S, Wang X, Chen T, Feng Z, Li C (2014) J Phys Chem C 118: 12661-12668

[70] Song G, Luo C, Fu Q, Pan C (2016) RSC Adv 6: 84035-84041

[71] Macak JM, Tsuchiya H, Ghicov A, Yasuda K, Hahn R, Bauer S, Schmuki P (2007) Curr Opin Solid St M 11:3-18

[72] Shankar K, Mor GK, Prakasam HE, Yoriya S, Paulose M, Varghese OK, Grimes CA (2007) Nanotechnology 18 (065707):1-11

[73] Aurora P, Rhee P, Thompson L (2010) J Electrochem Soc 157:K152-K155

[74] Altomare M, Lee K, Killian MS, Selli E, Schmuki P (2013) Chem Eur J 19:5841-5844

[75] Thimsen E, Rastgar N, Biswas P (2008) J Phys Chem C 112:4134-4140

[76] Palmas S, Da Pozzo A, Mascia M, Vacca A, Ricci PC, Matarrese R (2012) J Solid State Electrochem 16:2493-2502

[77] Palmas S, Da Pozzo A, Mascia M, Vacca A, Matarrese R (2012) Int J Photoenergy 914757:1-7

Tables captions

Table 1. Circuit parameters obtained by fitting the experimental impedance results with the selected equivalent circuit for PLD samples deposited at 3, 5 and 10 Pa. Data obtained under dark conditions at -0.7V.

Table 2. Circuit parameters obtained by fitting the experimental impedance results with the selected equivalent circuit for PLD samples deposited at 3, 5 and 10 Pa. Data obtained under illumination (365nm wavelenght) at 0.5V.

	3 Pa	**5 Pa**	**10 Pa**
C_1 (C)	1.52E-07	1.29E-07	2.12E-07
$R_1(\Omega)$	20.78	20.08	15.34
τ_1 (s)	3.16E-06	2.58E-06	3.26E-06
Q_2 ($S\ s^n$)	4.53E-05	1.00E-04	9.49E-05
n_2	0.6874	0.6608	0.6786
$R_2(\Omega)$	2.23E+04	793.4	1.16E+04
τ_2 (s)	1.02	0.02	1.15
C_3 (C)	3.03E-05	1.14E-04	6.80E-05
R_3 (Ω)	43.11	1462	149.3
τ_3 (s)	0.0013	0.1665	0.0102

Table 1

	3 Pa	5 Pa	10 Pa
$Q_1(S\ s^n)$	6.54E-08	1.18E-07	1.05E-07
n_1	1	0.95	1
$R_1(\Omega)$	24.32	24.61	21.56
$\tau_1(s)$	1.59E-06	1.48E-06	2.26E-06
$Q_2(S\ s^n)$	2.27E-05	1.88E-05	3.36E-05
n_2	0.78	0.81	0.86
$R_2(\Omega)$	9608	6910	5135
$\tau_2(s)$	0.14	0.08	0.13
$Q_3(S\ s^n)$	7.45E-06	6.68E-06	1.03E-05
n_3	0.97	1	0.92
$R_3(\Omega)$	1.02E+05	2.58E+05	2.74E+05
$\tau_3(s)$	0.75	1.72	3.11

Table 2

Figures captions

Fig 1. SEM images of as deposited PLD grown TiO_2 photoanodes produced with mass=0.5*M* and at different background gas pressure: a=3 Pa, b=5 Pa, c=10 Pa, d=15 Pa O_2.

Fig 2. Film density variation (black squares and dotted line) and the related film porosity (red circles and solid line) of as deposited PLD grown TiO_2 photoanodes produced at different background gas pressure (mass=0.5*M*).

Fig 3. SEM images showing the effect of thermal treatment on PLD grown TiO_2 films deposited at 5 Pa and 10 Pa O_2 (mass=0.5*M*).

Fig4. Raman spectra of a compact film grown at 5 Pa O_2 (left) and a porous film grown at 10 Pa O_2 (right), as deposited (on glass substrate) and after annealing at 500, 650 and 800°C (on crystalline silicon substrate). Raman peaks related to anatase (rutile) phase are indicated by A (R). Silicon Raman peak at 521 cm^{-1} is indicated with a dashed line in the spectra of annealed films.

Fig 5. SEM images of the annealed TNT photoanode: top-view (a); cross-view (b).

Fig. 6. EIS results measured under dark conditions at -0.7V in 0.1M KOH for samples deposited at 3, 5 and 10 Pa pressure (annealed at 500°C, mass=0.5*M*): Nyquist plots

Fig 7. Comparison of reductive voltammetric scan performed under dark conditions in ferro/ferricyanide solution over samples deposited at 3, 5 and 10 Pa pressure (annealed at 500°C, mass=0.5*M*). Inset: example of whole voltammetric scan (potential scan rate 100 mV/s).

Fig 8. Current-potential response of the PLD grown TiO_2 photoanodes. Fig. 8a: Dark conditions (curve a); samples produced at 5 Pa pressure annealed at 500°C (curve b: mass=0.5*M*; curve c: mass=*M*; curve d: mass=2*M*), 650°C and 800°C (curve e and f (mass=0.5*M*)). Fig. 8b: samples produced at 3 Pa pressure, annealed at 500°C (curve a: mass=0.5*M*; curve b: mass=*M*) and 650°C (curve c: mass=0.5*M*). Fig. 8c: samples produced at 10 Pa pressure (mass=0.5*M*), annealed at 500, 650 and 800°C (curves a, b and c). Fig. 8d: samples produced at 15 Pa pressure

(mass=0.5*M*), annealed at 500, 650 and 800°C (curves a, b and c). Current-potential response of the TNT photoanode (Fig. 8b, curve d).

Fig 9. Photoelectrochemical behaviour for PLD grown TiO_2 photoanodes produced at different background pressure and annealed at 500 °C (White bars: mass=0.5*M*; Brown bars: mass=*M*; Gray bars: mass=2*M*). a: photopotential on-set; b: photocurrent densities measured at 0.5 V.

Fig 10. EIS results measured under illumination (365nm wavelenght) at 0.5V for for samples deposited at 3, 5 and 10 Pa pressure (annealed at 500°C, mass=0.5*M*): a) phase angle (empty symbols) and modulus (solid symbols) Bode plots; b) Nyquist plots

Fig 11. Photoconversion efficiency as a function of the applied potential. a: Effect of the background pressure for the PLD grown TiO_2 photoanodes annealed at 500 °C (mass=0.5*M*); b: Effect of thickness for the PLD grown TiO_2 photoanodes produced at 5Pa (annealing temperature = 500 °C; corresponding thicknesses reported in the figure) and photoconversion efficiency for the TNT photoanode); c: Effect of thickness for the PLD grown TiO_2 photoanodes produced at 3 Pa (annealing temperature = 500 °C; corresponding thicknesses reported in the figure): d: Effect of the background pressure for the PLD grown TiO_2 photoanodes annealed at 650 °C (mass=0.5*M*)

Fig 12. Photoelectrochemical behaviour for the PLD grown TiO_2 photoanodes produced at different background pressure and annealed at 650 °C (With bars) and 800 °C (Black bars): photocurrent densities measured at 0.5 V.

Fig 13. Photoelectrochemical behaviour in the presence of organic sacrificial reagents in terms of performance gain γ evaluated as ratio between the photocurrent values obtained 0.5 V with and without the organics as a function of their volume fraction (PLD grown TiO_2 photoanodes deposited at 5 Pa (mass=*M*) and annealed at 500 °C)

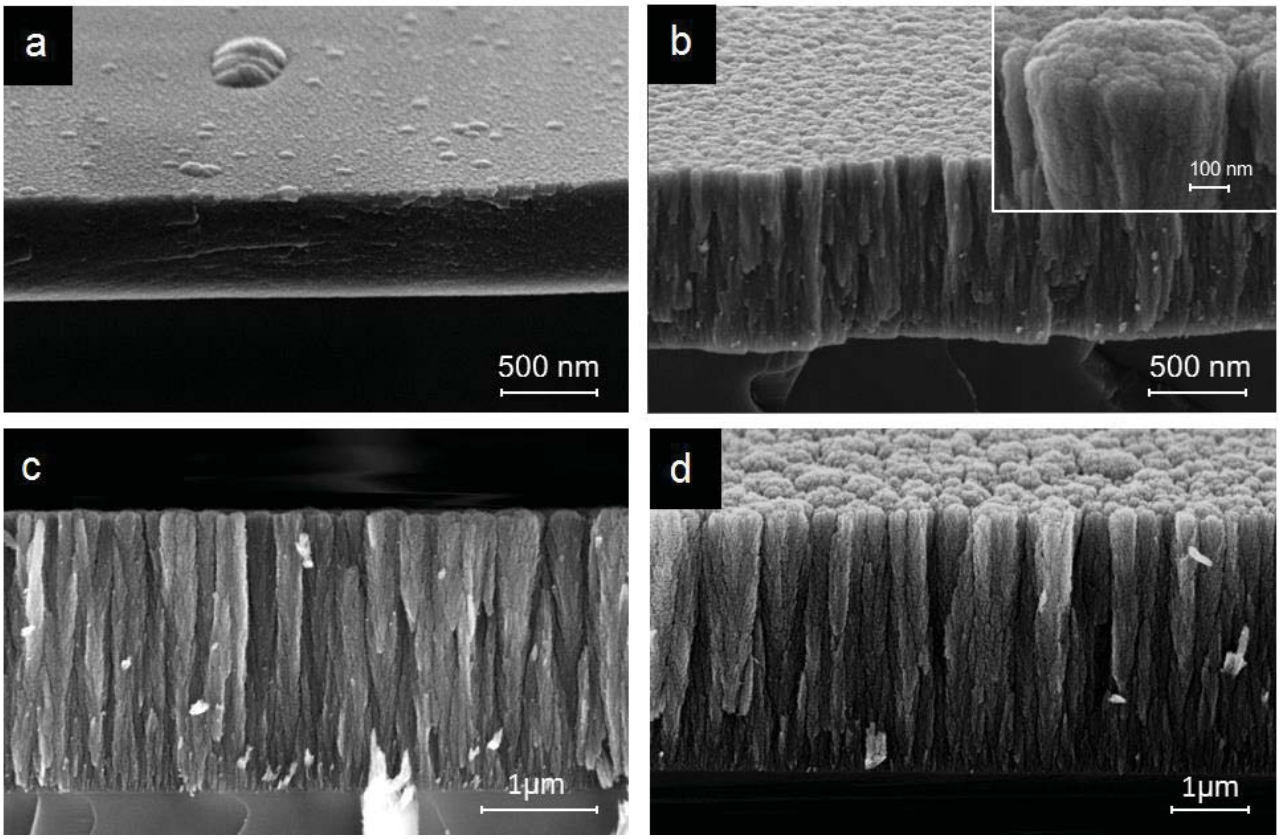

Fig 1.

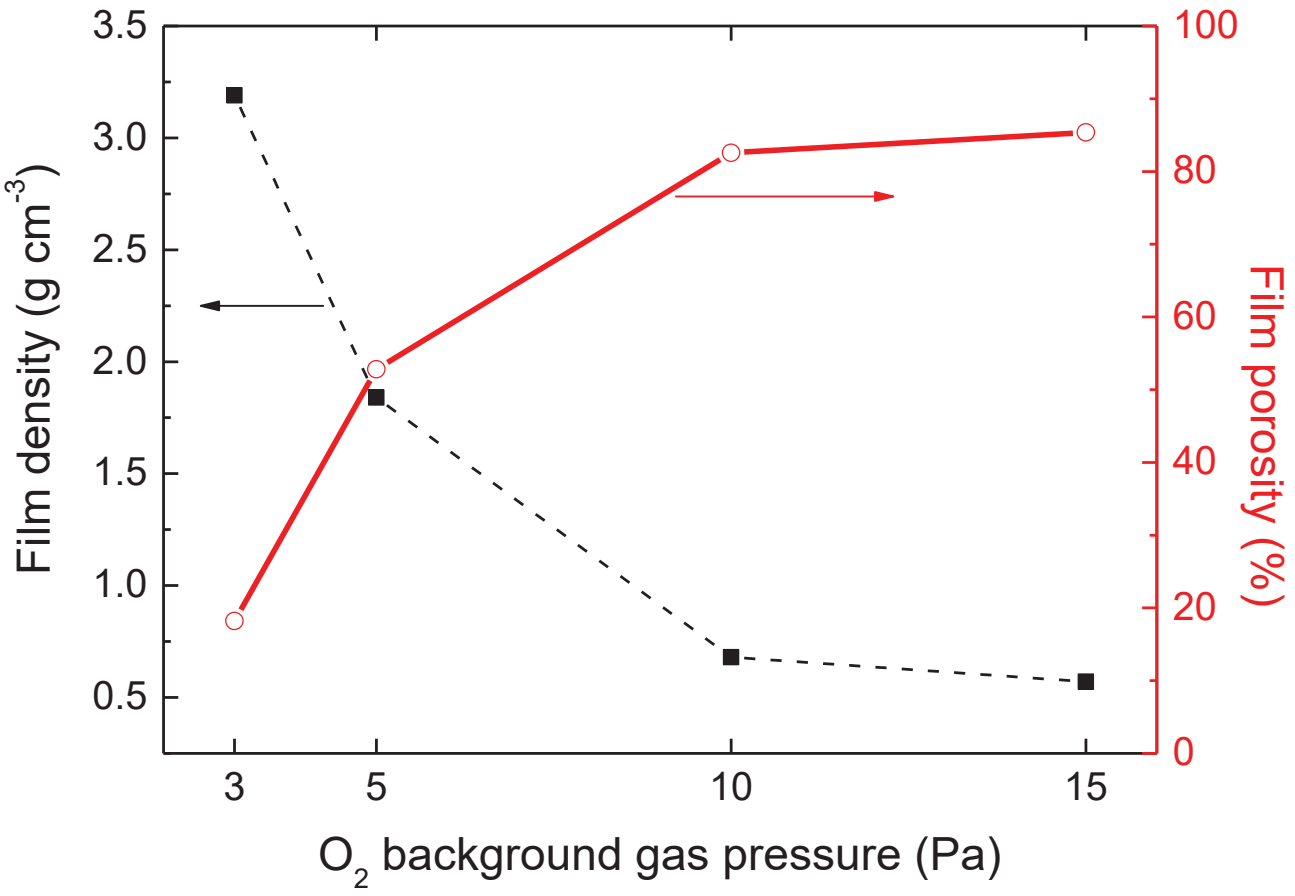
Film density (g cm-3)
Film porosity (%)
O2 background gas pressure (Pa)
3.5
3.0
2.5
2.0
1.5
1.0
0.5
100
80
60
40
20
0
3
5
10
15

Fig 2.

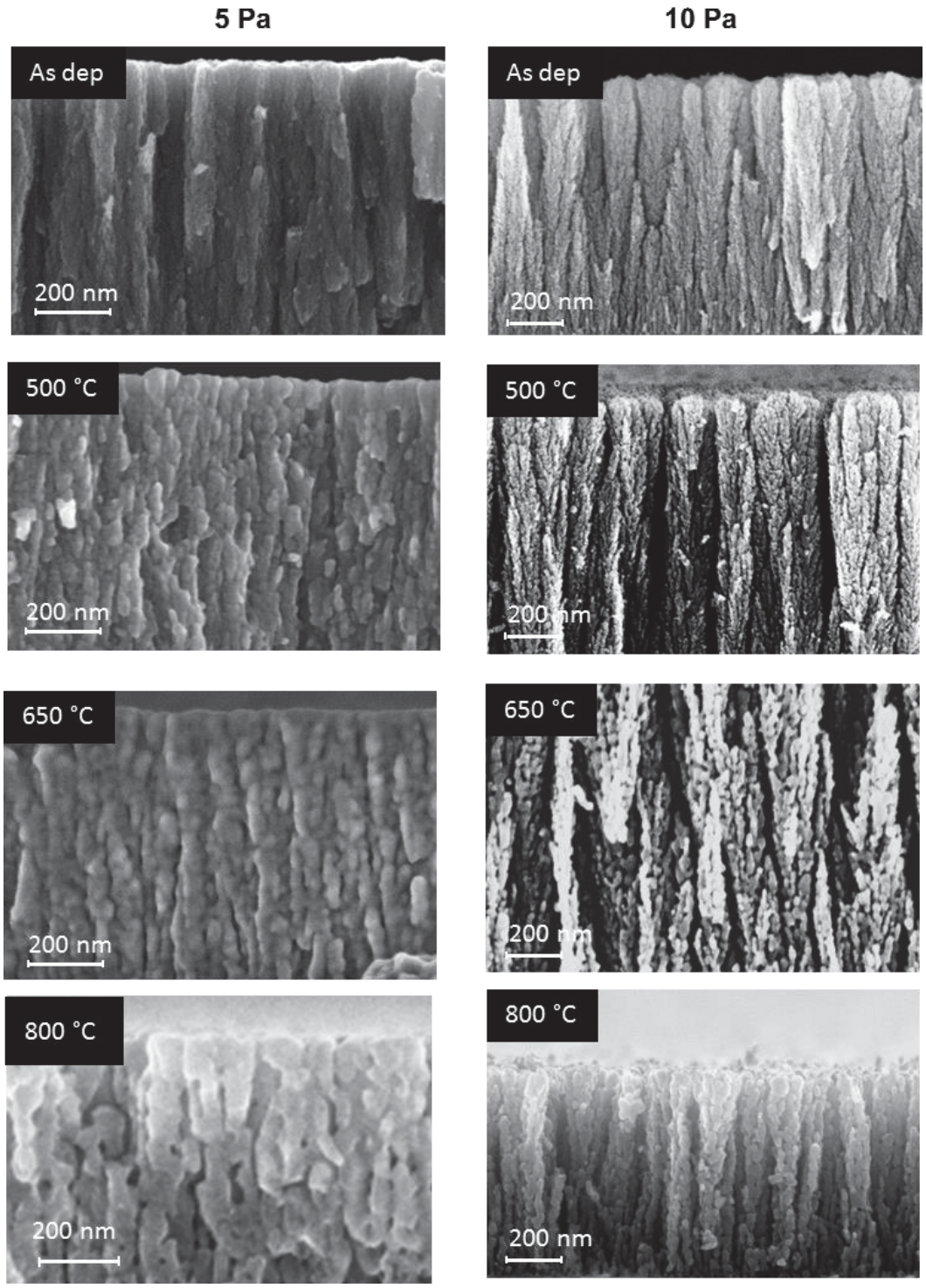
5 Pa
10 Pa
As dep
200 nm
As dep
200 nm
500 °C
200 nm
500 °C
200 nm
650 °C
200 nm
650 °C
200 nm
800 °C
200 nm
800 °C
200 nm

Fig 3.

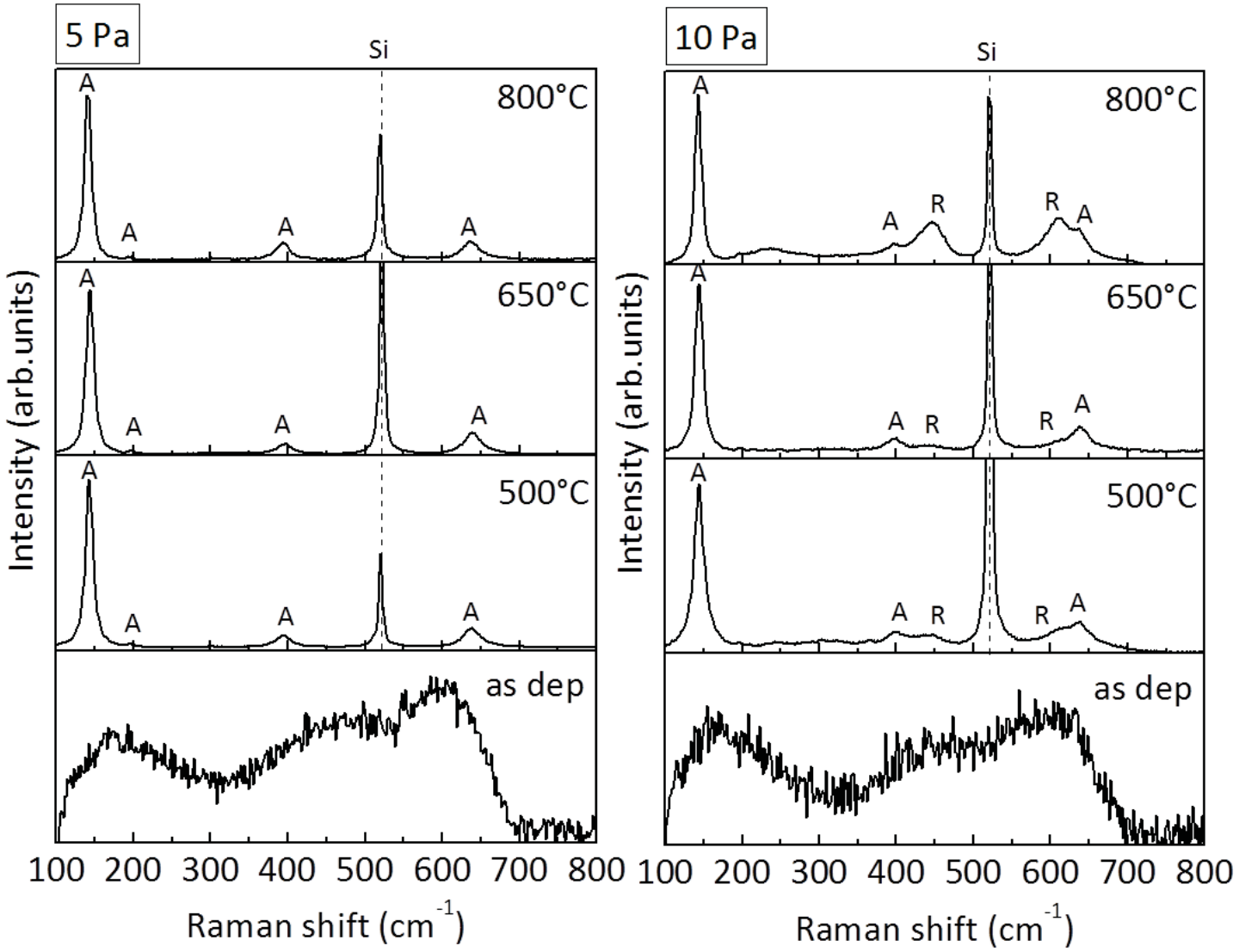
5 Pa
10 Pa
Si
800°C
650°C
500°C
as dep
A
R
Intensity (arb.units)
100 200 300 400 500 600 700 800
Raman shift (cm-1)

Fig 4.

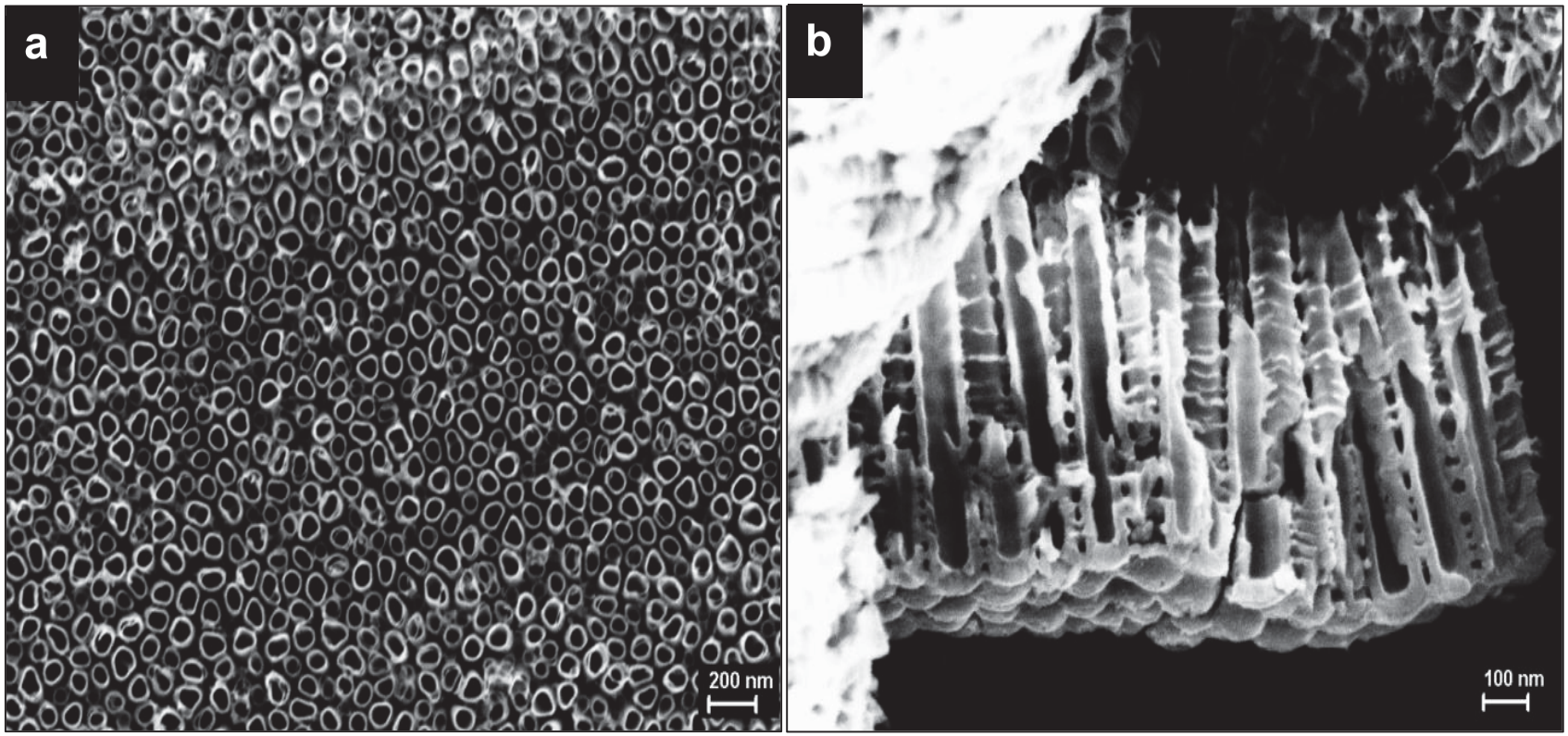

Fig 5.

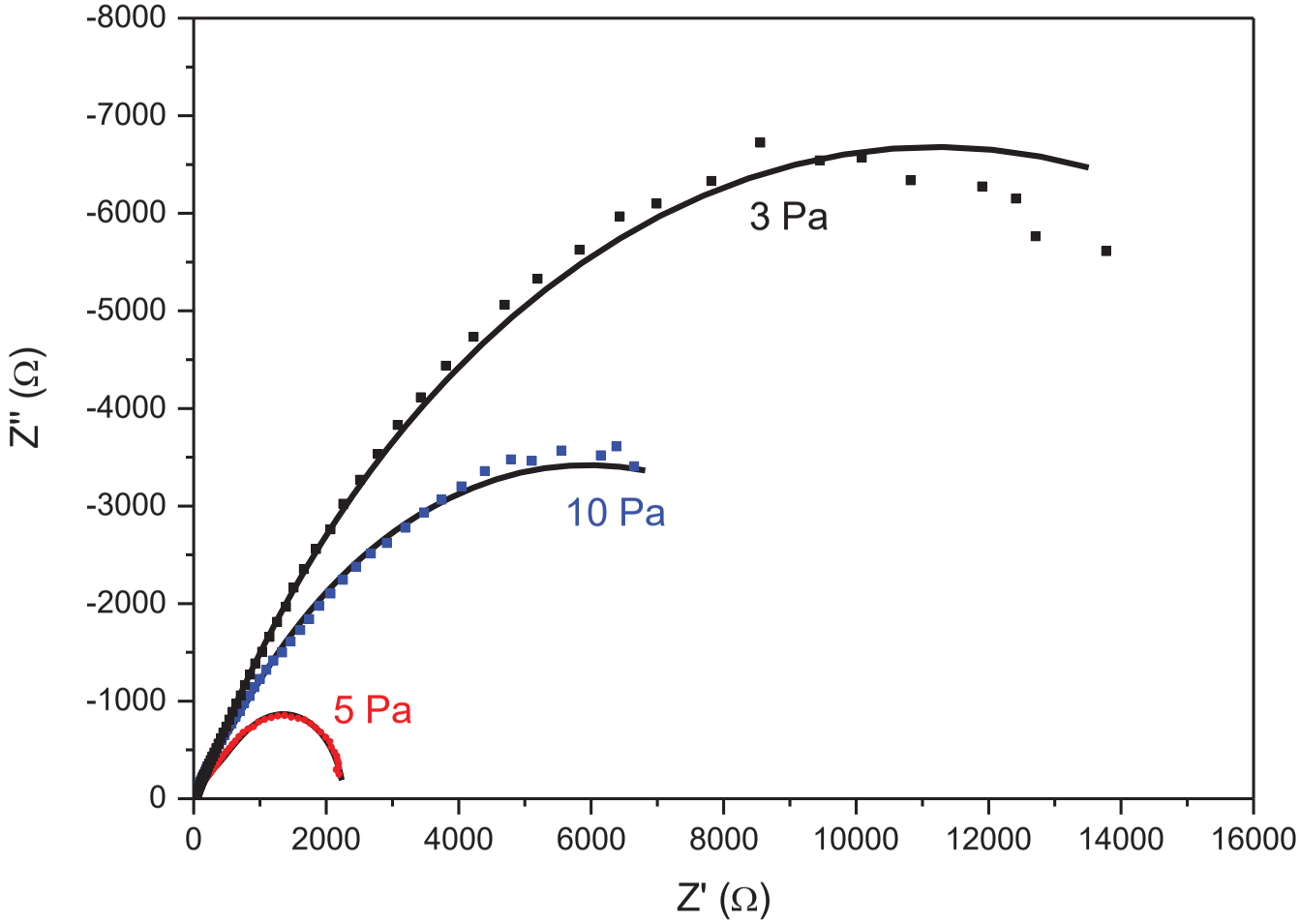
-8000
-7000
-6000
-5000
-4000
-3000
-2000
-1000
0
Z'' (Ω)
0
2000
4000
6000
8000
10000
12000
14000
16000
Z' (Ω)
3 Pa
10 Pa
5 Pa

Fig 6.

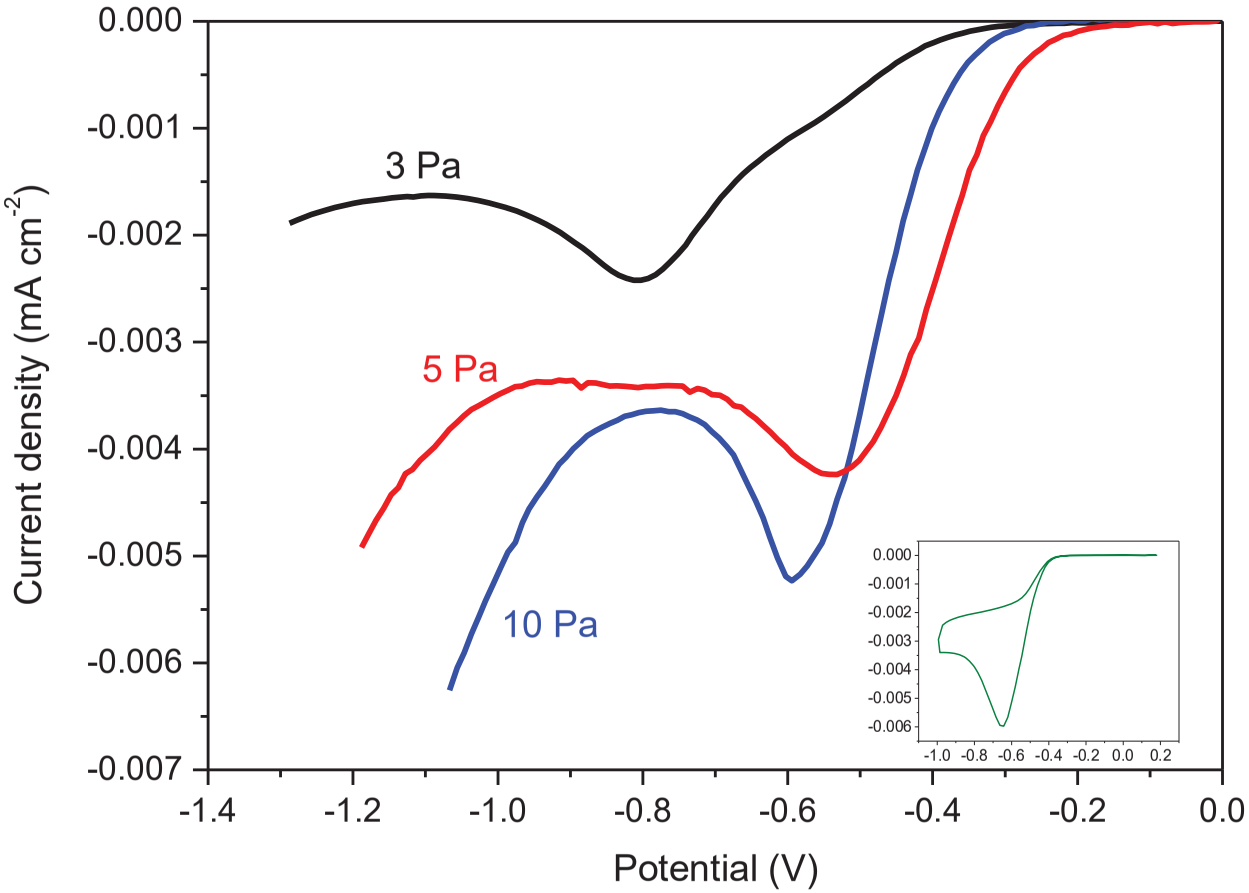
0.000
-0.001
-0.002
-0.003
-0.004
-0.005
-0.006
-0.007
Current density (mA cm-2)
-1.4
-1.2
-1.0
-0.8
-0.6
-0.4
-0.2
0.0
Potential (V)
3 Pa
5 Pa
10 Pa

Fig. 7

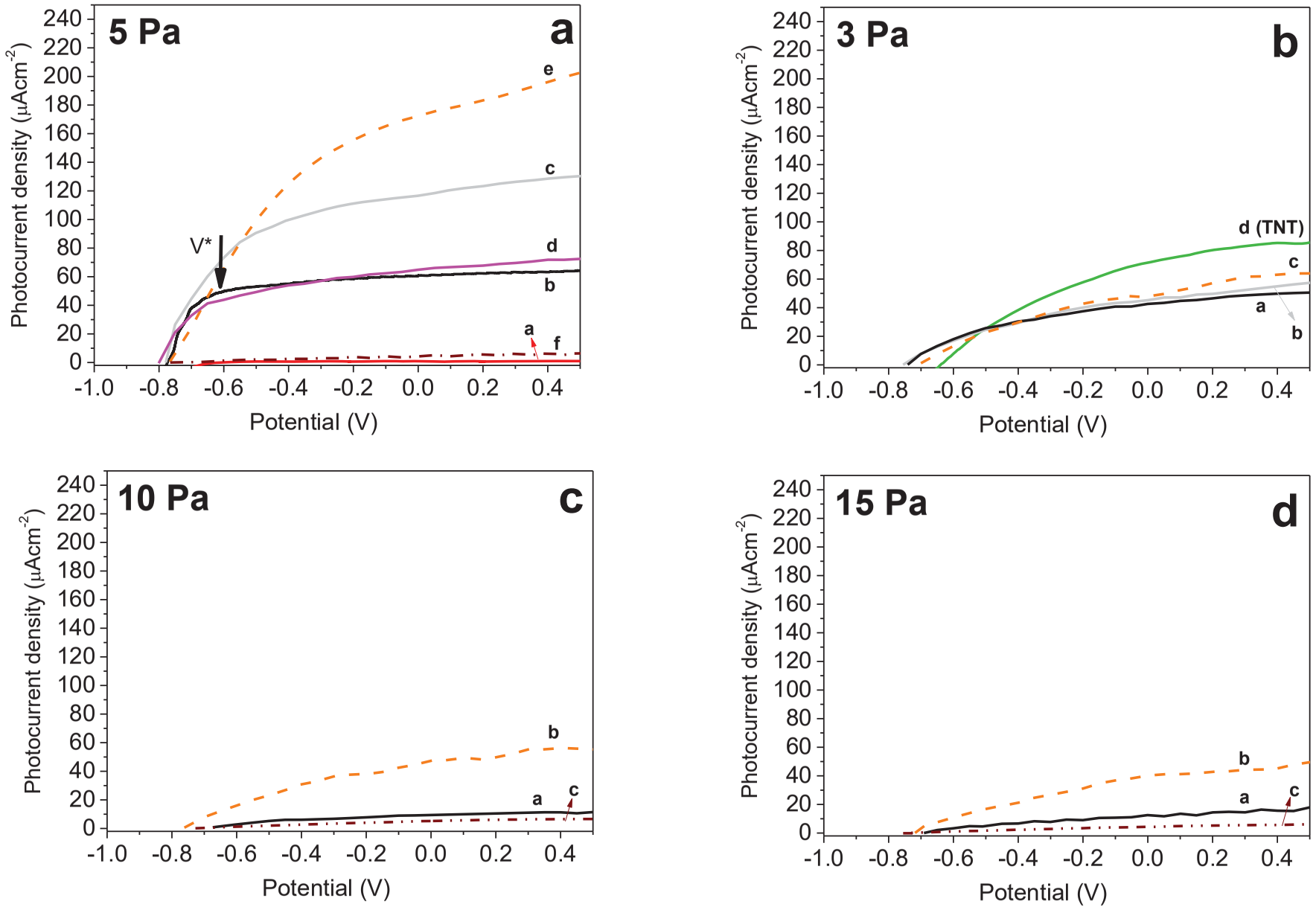
5 Pa
a
e
c
V*
d
b
a
f
Photocurrent density (μAcm-2)
Potential (V)
3 Pa
b
d (TNT)
c
a
b
10 Pa
c
b
a
c
15 Pa
d
b
a
c

Fig 8.

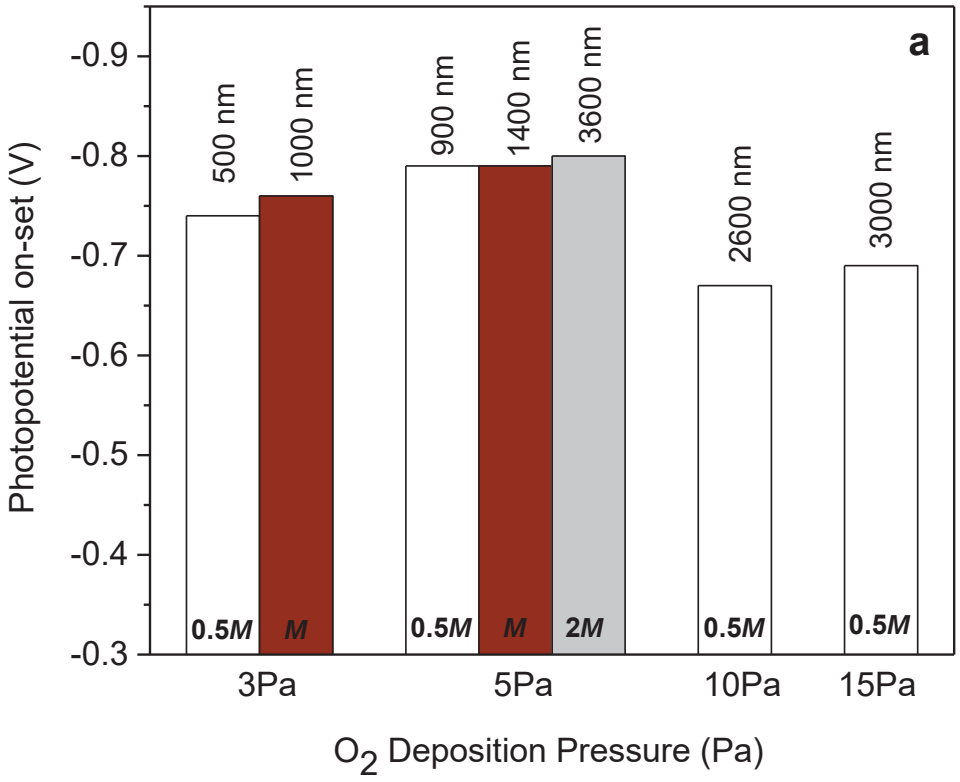
a
Photopotential on-set (V)
-0.9
-0.8
-0.7
-0.6
-0.5
-0.4
-0.3
500 nm
1000 nm
900 nm
1400 nm
3600 nm
2600 nm
3000 nm
0.5M
M
0.5M
M
2M
0.5M
0.5M
3Pa
5Pa
10Pa
15Pa
O2 Deposition Pressure (Pa)

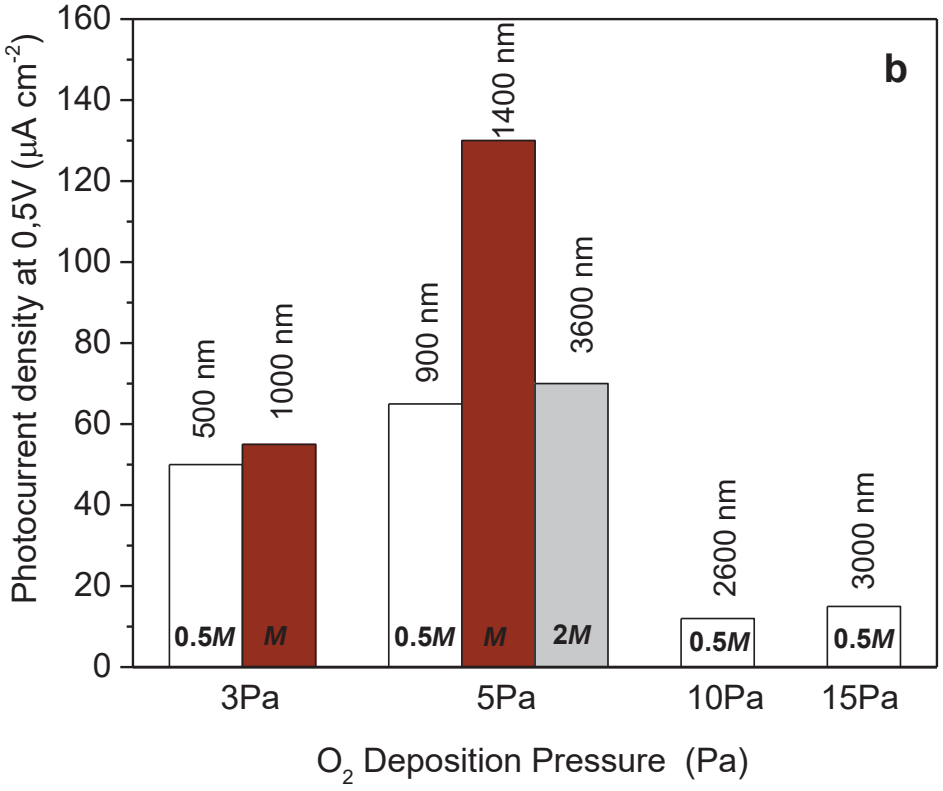
b
Photocurrent density at 0,5V (μA cm-2)
160
140
120
100
80
60
40
20
0
500 nm
1000 nm
900 nm
1400 nm
3600 nm
2600 nm
3000 nm
0.5M
M
0.5M
M
2M
0.5M
0.5M
3Pa
5Pa
10Pa
15Pa
O2 Deposition Pressure (Pa)

Fig 9.

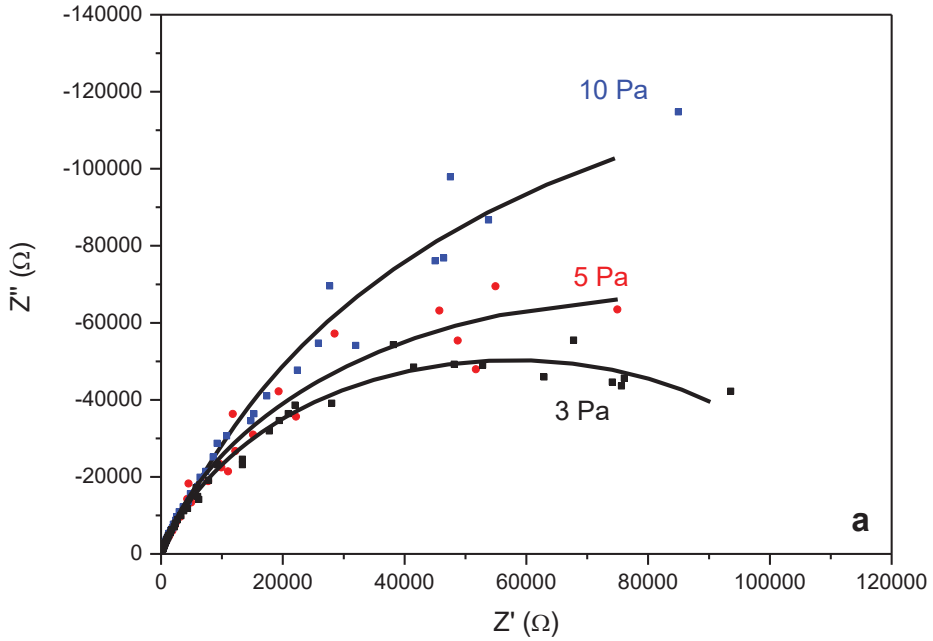
-140000
-120000
-100000
-80000
-60000
-40000
-20000
0
Z'' (Ω)
0
20000
40000
60000
80000
100000
120000
Z' (Ω)
10 Pa
5 Pa
3 Pa
a

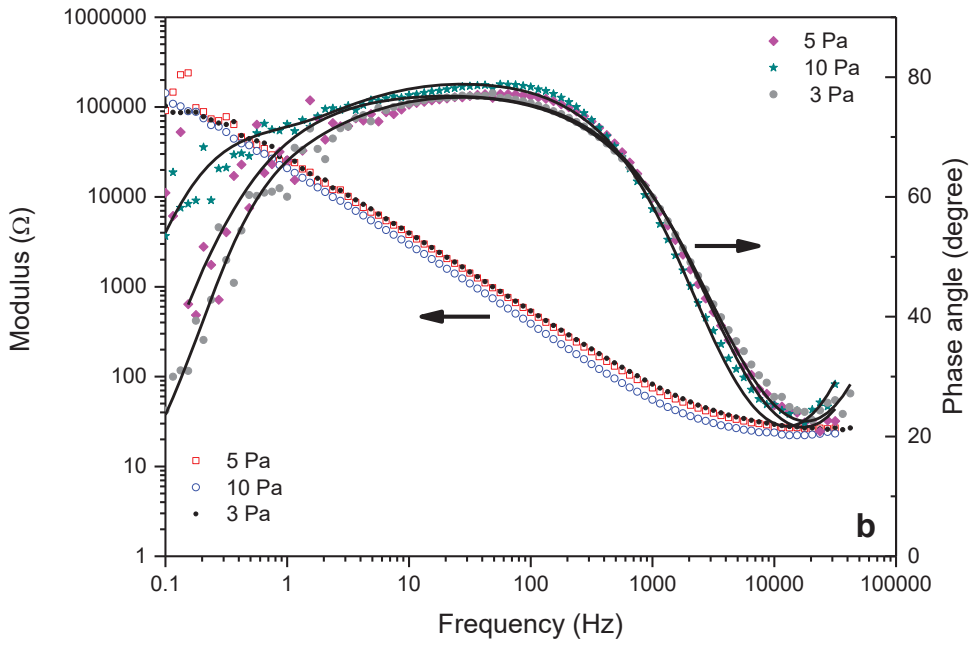
1000000
100000
10000
1000
100
10
1
Modulus (Ω)
0.1
1
10
100
1000
10000
100000
Frequency (Hz)
80
60
40
20
0
Phase angle (degree)
5 Pa
10 Pa
3 Pa
5 Pa
10 Pa
3 Pa
b

Fig 10.

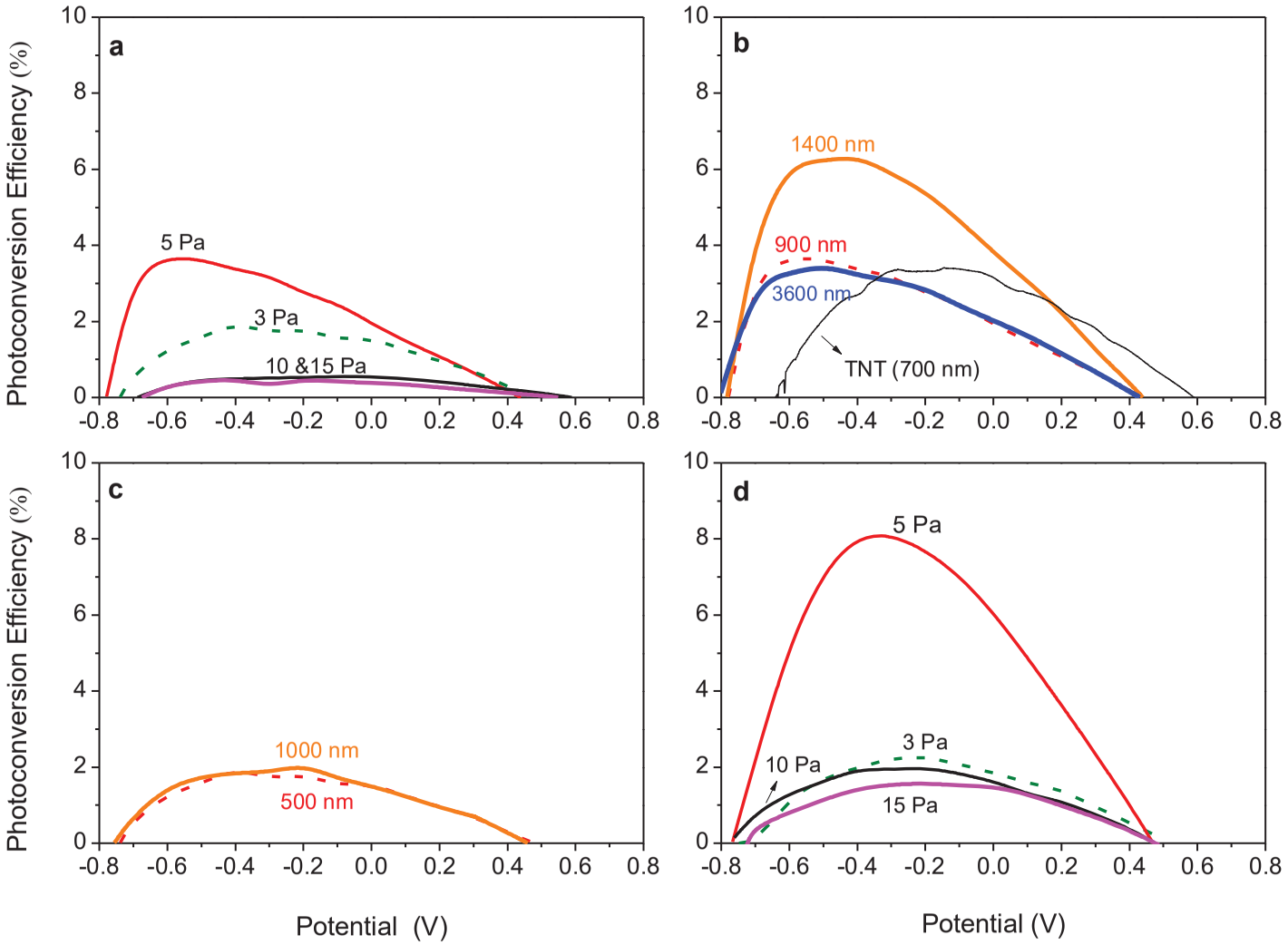
a
b
c
d
Photoconversion Efficiency (%)
Photoconversion Efficiency (%)
Potential (V)
Potential (V)
5 Pa
3 Pa
10 &15 Pa
1400 nm
900 nm
3600 nm
TNT (700 nm)
1000 nm
500 nm
5 Pa
10 Pa
3 Pa
15 Pa

Fig 11.

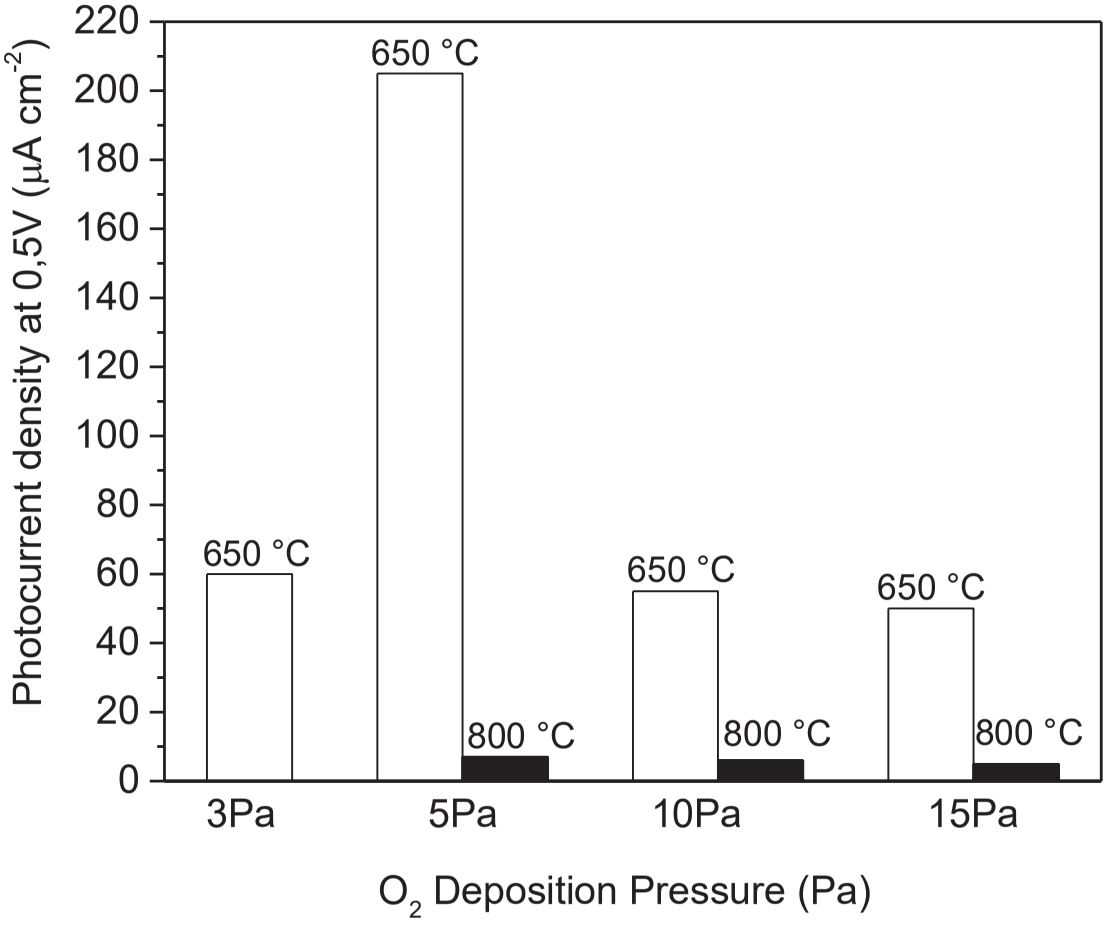
Photocurrent density at 0,5V (μA cm-2)
220
200
180
160
140
120
100
80
60
40
20
0
650 °C
650 °C
650 °C
650 °C
800 °C
800 °C
800 °C
3Pa
5Pa
10Pa
15Pa
O2 Deposition Pressure (Pa)

Fig 12.

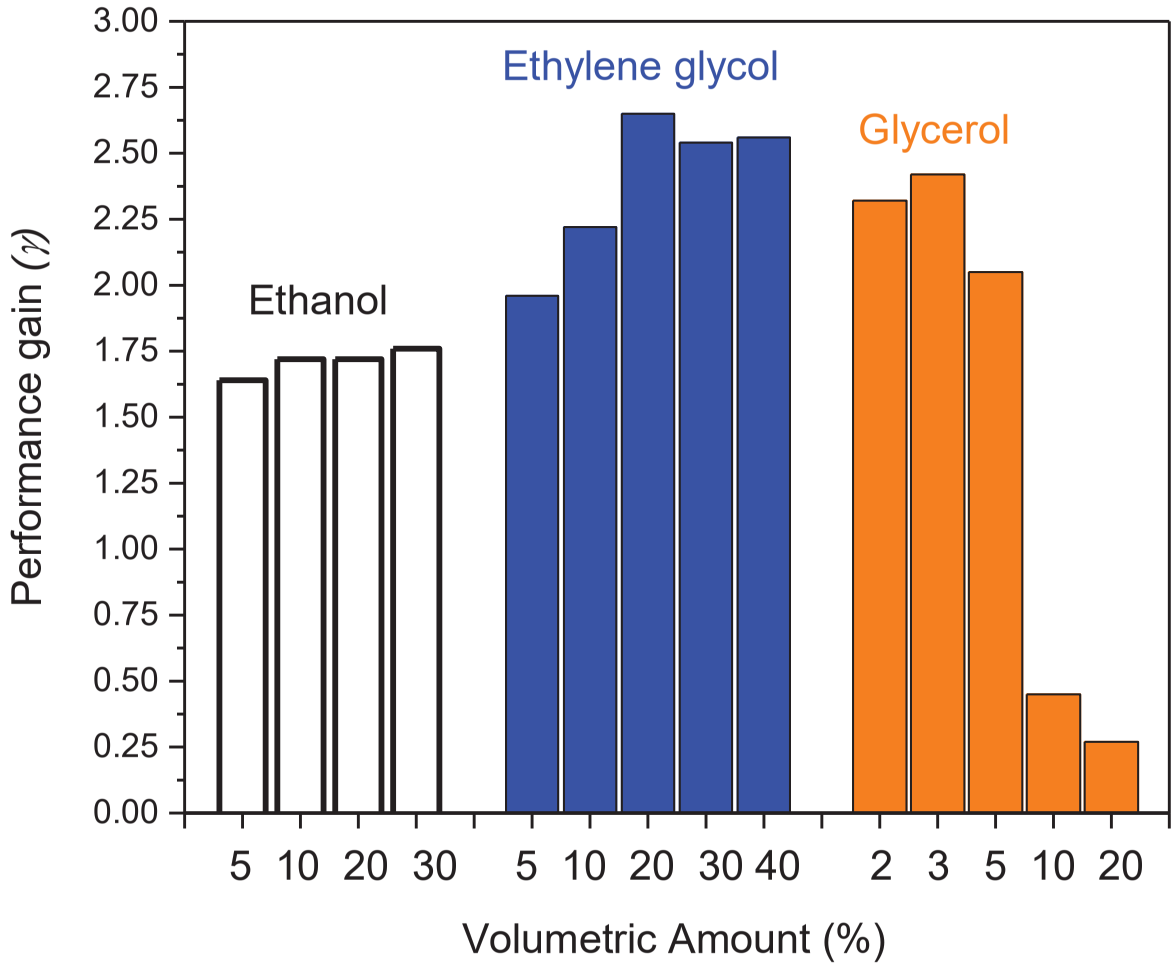
Performance gain (γ)
3.00
2.75
2.50
2.25
2.00
1.75
1.50
1.25
1.00
0.75
0.50
0.25
0.00
Ethylene glycol
Glycerol
Ethanol
5 10 20 30 5 10 20 30 40 2 3 5 10 20
Volumetric Amount (%)

Fig 13.